Draft version March 18, 2024
Typeset using LaTeX default style in AASTeX63

CHEMICAL COMPOSITIONS OF RED GIANT STARS FROM HABITABLE ZONE PLANET FINDER SPECTROSCOPY

Christopher Sneden,[1] Melike Afşar,[2,1] Zeynep Bozkurt,[3] Gamze Böcek Topcu,[4] Sergen Özdemir,[5] Gregory R. Zeimann,[6] Cynthia S. Froning,[7] Suvrath Mahadevan,[8,9] Joe P. Ninan,[10,9] Chad F. Bender,[11] Ryan Terrien,[12] Lawrence W. Ramsey,[13,9] Karin Lind,[14] Gregory N. Mace,[15] Kyle F. Kaplan,[16] Hwihyun Kim,[17] Keith Hawkins,[18] and Brendan P. Bowler[19]

[1] *Department of Astronomy and McDonald Observatory, The University of Texas, Austin, TX 78712, USA; chris@verdi.as.utexas.edu*
[2] *Department of Astronomy and Space Sciences, Ege University, 35100 Bornova, İzmir, Turkey; melike.afsar@gmail.com*
[3] *Department of Astronomy and Space Sciences, Ege University, 35100 Bornova, İzmir, Turkey; zeynep.bozkurt@ege.edu.tr*
[4] *Department of Astronomy and Space Sciences, Ege University, 35100 Bornova, İzmir, Turkey; gamzebocek@gmail.com*
[5] *Department of Astronomy and Space Sciences, Ege University, 35100 Bornova, İzmir, Turkey; sergenozdemir58@gmail.com*
[6] *Hobby Eberly Telescope, The University of Texas, Austin, TX 78712, USA; gregz@astro.as.utexas.edu*
[7] *Department of Astronomy and McDonald Observatory, The University of Texas, Austin, TX 78712, USA; cfroning@astro.as.utexas.edu*
[8] *Department of Astronomy & Astrophysics, The Pennsylvania State University, University Park, PA 16803, USA; suvrath@astro.psu.edu*
[9] *Center for Exoplanets and Habitable Worlds, The Pennsylvania State University, University Park, PA 16803, USA*
[10] *Department of Astronomy & Astrophysics, The Pennsylvania State University, University Park, PA 16803, USA; jpn23@astro.psu.edu*
[11] *Department of Astronomy and Steward Observatory, University of Azizona, Tucson, AZ 85721, USA; bender@email.arizona.edu*
[12] *Department of Physics and Astronomy, Carleton College, Northfield, MN 55057, USA; rterrien@carleton.edu*
[13] *Department of Astronomy & Astrophysics, The Pennsylvania State University, University Park, PA 16803, USA; lwr@astro.psu.edu*
[14] *Department of Astronomy, Stockholm University, AlbaNova University Centre, SE-106 91 Stockholm, Sweden: karin.lind@astro.su.se*
[15] *Department of Astronomy and McDonald Observatory, The University of Texas, Austin, TX 78712, USA; gmace@astro.as.utexas.edu*
[16] *SOFIA Science Center, NASA Ames Research Center, Mail Stop N232−12 P.O. Box 1, Moffett Field, CA 94036, USA; kkaplan@usra.edu*
[17] *Gemini Observatory, Casilla 603, La Serena, Chile; hkim@gemini.edu*
[18] *Department of Astronomy and McDonald Observatory, The University of Texas, Austin, TX 78712, USA; keithhawkins@utexas.edu*
[19] *Department of Astronomy and McDonald Observatory, The University of Texas, Austin, TX 78712, USA; bpbowler@astro.as.utexas.edu*

ABSTRACT

We have used the Habitable Zone Planet Finder (HPF) to gather high resolution, high signal-to-noise near-infrared spectra of 13 field red horizontal-branch (RHB) stars, one open-cluster giant, and one very metal-poor halo red giant. The HPF spectra cover the 0.81−1.28 μm wavelength range of the zyJ bands, filling in the gap between the optical (0.4−1.0 μm) and infrared (1.5−2.4 μm) spectra already available for the program stars. We derive abundances of 17 species from LTE-based computations involving equivalent widths and spectrum syntheses, and estimate abundance corrections for the species that are most affected by departures from LTE in RHB stars. Generally good agreement is found between HPF-based metallicities and abundance ratios and those from the optical and infrared spectral regions. Light element transitions dominate the HPF spectra of these red giants, and HPF data can be used to derive abundances from species with poor or no representation in optical spectra (e.g., C I, P I, S I, K I). Attention is drawn to the HPF abundances in two field solar-metallicity RHB stars of special interest: one with an extreme carbon isotope ratio, and one with a rare very large lithium content. The latter star is unique in our sample by exhibiting very strong He I 10830 Å absorption. The abundances of the open cluster giant concur with those derived from other wavelength regions. Detections of C I and S I in HD 122563 are reported, yielding the lowest metallicity determination of [S/Fe] from more than one multiplet.

Corresponding author: Christopher Sneden
chris@verdi.as.utexas.edu

Keywords: stellar abundances - horizontal branch stars - evolved stars

1. INTRODUCTION

Red horizontal branch (RHB) stars (also called "secondary red clump"; e.g., Girardi et al. 1998, Girardi 1999, Ruiz-Dern et al. 2018) are mostly known for their prominent locations on the Hertzsprung-Russell (HR) diagrams of globular clusters. They are evolved stars with double energy sources, burning helium in the core and hydrogen burning in the shell. RHB stars are not easy to identify among field stars, but their cooler counterparts, the red clump (RC) stars, are relatively more numerous and have narrowly constrained temperatures and gravities, making them stand out in color-magnitude diagrams. RHB and RC stars have small luminosity ranges, and thus can serve as standard candles.

Accurate chemical compositions of RHB stars along with robust statistics of their occurrence in disk and halo populations can enhance our knowledge of stellar and Galactic evolution. RHBs are important astrophysical tools that can be used to study stellar densities, kinematics, and chemical abundances across the Galactic disk, and allow us to reach out greater distances than the dwarfs or other regular giants would provide (e.g. Girardi 2016). Afşar et al. (2018a) (here after Afşar18a) have studied the detailed chemical compositions and kinematics of a sample of 340 candidate field RHB stars in the optical spectral region (3400−10900 Å). Their chemo-kinematical analysis of these candidates revealed the presence of more than 150 field RHB and RC stars, located both in the thin and thick disk of the Galaxy. Later, Afşar et al. (2018b) (hereafter Afşar18b) investigated three RHB stars in detail using high-resolution H- and K-band (1.48−2.48 μm) spectra obtained with the Immersion Grating Infrared Spectrograph (IGRINS). In that work they argued that in general the IR and optical abundances agree well, and for some elements (e.g., Mg, Si) the IR abundances are more trustworthy than the optical ones. Additionally, that work highlighted the abundances of several elements (e.g., P, S, K) with prominent transitions in the IR whose optical lines are too weak to be detected or too strong to yield reliable abundances.

Our work investigates some selected RHB stars from Afşar2018a,b in the relatively under-studied zyJ wavelength region, using high-resolution spectra obtained with the Habitable Zone Planet Finder (HPF) spectrograph. We derive metallicities and abundances of 13 RHB stars. We also report on our analyses of the well-known very metal-poor halo red giant, HD 122563 (Afşar et al. 2016 and references therein, hereafter Afşar16), and of one red giant member from open cluster NGC 6940 (MMU 105; Böcek Topcu et al. 2016, Böcek Topcu et al. 2019, here after BT16, and BT19). These two stars will be considered separately from the discussion of the RHB stars.

In §2 we introduce the stellar sample, describe HPF, and outline the observations and reductions. Atomic and molecular line selection, equivalent width measurements, synthetic spectrum computations, and abundance derivations are given in §3. We consider four stars with noteworthy abundance signatures in §4, and conclude with our summary in §5.

2. OBSERVATIONS AND REDUCTIONS

The red giants investigated in this HPF spectroscopic study (Table 1) have been selected from our previous studies (Afşar16,18a,b, BT16,19). See those papers for detailed descriptions of the optical and IGRINS observations of our program stars. In general the HPF zyJ wavelength domain has been relatively neglected in stellar abundance studies. In order to sample spectra of red giants in this region, we have selected stars with various chemical composition characteristics. The following sub-sections focus on the details of HPF observations.

2.1. *HPF Spectra*

HPF is a high−resolution ($\lambda/\Delta\lambda \equiv R \sim 55{,}000$) near−infrared ($zyJ$ photometric bands, 8100−12800 Å) spectrograph on the 10m Hobby Eberly Telescope (HET) at McDonald Observatory (Mahadevan et al. 2012, 2014).[1] The main HPF goal is to search for exoplanets of cool M dwarf stars by detecting the orbital reflex motions of the parent stars. To achieve high velocity precision ($\sim$1.5 m s^{-1}), the entire HPF instrument is encased in a vacuum chamber cooled to 180 Kelvin, yielding temperature stability of $\sim$ 1 mK. The instrument has input fiber scrambling (Roy et al. 2014),

[1] https://hpf.psu.edu/

and precise wavelength characterization with a laser frequency comb (Halverson et al. 2014; Metcalf et al. 2019). At present HPF has generated studies of exoplanet systems and precision radial velocity techniques, but it has not been routinely applied to investigation of the atmospheres of stars warmer than spectral type M.

High-resolution, high signal-to-noise ($S/N > 100$) HPF spectra of 15 target stars were gathered over several months using the fully queue-scheduled HET (Shetrone et al. 2007). Table 1 gives basic data for these stars, and for warm, rapidly rotating, mostly featureless stars used as telluric divisors. In the zyJ spectral region the telluric molecular blockage ranges from near zero to almost total, varying significantly with wavelength. The dominant telluric contaminators are H_2O bands, and their contamination can change substantially on timescales of minutes, usually requiring a hot-star observation to accompany each target star. Some mitigation is provided by the fixed altitude of the HET, which on stable nights can lead to successful use of divisor star spectra acquired some time before or after the target spectra.

HPF observations of target and telluric warm stars were reduced using the HPF pipeline code *Goldilocks*.[2] This package processed the raw HPF data by removing bias noise, correcting for nonlinearity, masking cosmic rays, and calculating the slope/flux and variance image using the algorithms from the pyhxrg module in the tool *HxRGproc* (Ninan et al. 2018). The pipeline also processed bright lamp exposures to combine into a master frame to model the trace of the calibration, sky, and science fibers as well as their respective fiber profiles. The profiles were used as weights in an optimal extraction algorithm (Horne 1986) to produce 1D spectra and their associated propagated errors for all 28 orders. The master frame was also used to correct flat fielding features.

Goldilocks uses a single wavelength solution for all observations from the well-calibrated NIR Laser Frequency Comb. HPF's wavelength solution is extremely stable but does drift on the order of ∼10-20 m s^{-1} throughout the night with long term drifts over months on the same scale. This amounts to ∼1/100th of a pixel. Although *Goldilocks* provides the drift correction in the observation file headers, it is only important for precision radial velocity studies; we ignored this very small effect in our analysis.

For each stellar source, the science fiber extractions from *Goldilocks* includes light from the target as well as OH emission from the night sky. The sky fiber, located 50.1″away, contains only night sky emission. In most cases, the relative flux ratio between the sky emission and stellar continuum (at the wavelengths of interest) is less than 5%, and the sky emission has almost no effect on the target spectrum. In those situations we used the spectra of targets as extracted from the science fibers without attempting sky subtraction. For a few small spectral regions in which sky subtraction was critical to accurate representation of the stellar spectra, we performed the sky subtraction manually using the pipeline-extracted star and sky spectra.

After these reduction procedures, we performed continuum normalization of the target spectra via the *continuum* task of IRAF[3], and we used the *telluric* task to divide out the telluric contamination from the science target spectra. Later, individual orders were merged into a single continuous spectrum with the *scombine* task.

The *Goldilocks* pipeline produces rest wavelength solutions that are accurate to levels far beyond what are needed for our study. To measure the radial velocities (RVs) of our stellar targets we made use of *rv* package in IRAF. First we created synthetic spectra (as outlined in §3.1) adopting similar $T_{\rm eff}$, log g, and [Fe/H] values to our program stars. Then we used *rvcorrect* for the heliocentric corrections, and measured the RV values with the cross-correlation task *fxcor* (Fitzpatrick 1993). We only worked on the wavelength regions that are not affected (or only affected minimally) by the atmospheric telluric lines: 8420−8520 Å, 8540−8640 Å, 8660−8760 Å, 10275−10400 Å and 10450−10575 Å. We list the RVs from HPF and their standard deviations (σ) for each star in Table 2. The σ values were calculated by taking the average of RVs measured from individual regions listed above. Previous RV measurements of the same targets (Afşar18a and *Gaia* DR2) are also listed in Table 2 for comparison purposes.

The internal RV accuracies (line-to-line scatters) for individual stars are comparable: $\langle\sigma_{HPF}\rangle$ = 0.18 km s^{-1} and $\langle\sigma_{opt}\rangle$ = 0.19 km s^{-1}, and the velocity scales agree: $\langle RV_{opt}$-$RV_{HPF}\rangle$ = +0.45 ± 0.51 km s^{-1} (σ = 1.96 km s^{-1}). Our program stars also have RVs in the Gaia Data Release 2 Catalog (Arenou et al. 2018),and we list them also in Table 2. The agreement betwen HPF and Gaia is very good: $\langle RV_{opt}$-$RV_{Gaia}\rangle$ = −0.27 ± 0.08 km s^{-1} (σ = 0.31 km s^{-1}).

2.2. *Other Spectra*

[2] https://github.com/grzeimann/Goldilocks_Documentation

[3] http://iraf.noao.edu/

Our program stars have all had previous extensive analyses from optical region spectra. As described in detail by Afşar18a, the aHB high-resolution spectra were obtained with the Robert G. Tull Cross-Dispersed Echelle spectrograph (Tull et al. 1995) on the McDonald Observatory 2.7m Harlan J. Smith telescope. The instrumental setup yielded a spectral resolving power of $R = 60{,}000$ with effective wavelength coverage for the RHB observations of 4100−9000 Å. Redward of 5000 Å the S/N values always exceeded 100. The Tull Spectrograph was also used to obtain a very high S/N spectrum of the very metal-poor HD 122563. The optical spectrum for open cluster giant NGC 6940 MMU 105 was acquired with the High Resolution Spectrograph (Tull 1998) of the Hobby-Eberly Telescope at McDonald Observatory. It was configured to cover the spectral range 5100−6900 Å, with the same resolving power as our 2.7m Tull Spectrograph data.

A few of our HPF stars have also been observed at high resolution in the infrared H and K bands with the Immersion Grating Infrared Spectrometer (IGRINS; Yuk et al. 2010; Park et al. 2014) when this portable instrument was located at the McDonald Observatory 2.7m telescope. The IGRINS spectra for these bright RHB stars covered a wavelength range 14,800−24,800 Å, had resolving power $R \simeq 45{,}000$, and achieved $S/N \geq 150$. Our metallicity and abundance ratio analysis was reported by Afşar18b.

3. ABUNDANCE ANALYSES

3.1. *Line Lists*

In this exploration of HPF spectra of red giants we first sought to identify all useful atomic and molecular transitions for abundances analysis. HPF spectra cover the zyJ wavelength range 8170−12780 Å (0.82−1.28 μm). In RHB stars this spectral region contains many atomic lines, nearly all of which arise from light and Fe−group elements. In Figure 1 we show one of the HPF spectral orders that has several strong neutral−species lines of Na, Si, Ca, Fe, and Cr, one of the H I Paschen series lines, Fe II 10862.65 Å, and Sr II 10914.87 Å. The Sr II line and its multiplet partners at 10036.66 and 10327.31 Åare zyJ region rarities: ionized-species neutron-capture element ($Z > 30$) transitions. Neutron−capture elemental transitions are rarely strong enough in our stars for detection in this wavelength domain. A few Fe−group ionized species lines can be seen in red giant stars, but only one Fe II multiplet is strong enough for abundance analysis in our program stars.

There are also many molecular features in the zyJ region: OH ground state $^1\Sigma^+$, CO ground state $X^2\Pi$ rovibrational, and CN $A^2\Pi - X^2\Sigma^+$ red system transitions. But in general only CN lines have large absorption strengths. They can significantly contaminate many otherwise useful atomic transitions. In practice this problem forces examination of each potential atomic line for the presence of blends.

With potential line contamination issues, we chose candidate atomic features for abundance analysis by comparing HPF data in each spectral order with synthetic spectra for RHB star HIP 114809. Detailed matching of synthetic and observed spectra was not sought at this point. For all computations of synthetic spectra and predicted single-line equivalent widths (EWs) in this paper we used the current version of the LTE plane-parallel line analysis code MOOG (Sneden 1973)[4]. The input atomic and molecular line lists were generated by the auxiliary code *linemake*[5]. We adopted the model atmosphere for HIP 114809 derived for the RHB survey by Afşar18a, and whose parameters are given in Table 3. By this process we identified useful transitions of 16 elements; 14 of these have only neutral-species lines. A single Ti II line was detected, along with the very strong Sr II lines mentioned above.

In Table 4 we list the atomic lines chosen for this study. A fundamental limitation of abundance analyses in the zyJ spectral region is the lack of substantial sets of reliable transition probabilities based on laboratory spectroscopy. For this initial HPF abundance study of RHB stars we decided to avoid deriving empirical $\log(gf)$ values from the observed solar spectrum, as their values are difficult to disentangle from choices of solar model atmosphere, line damping parameters, and solar microturbulent velocity. The Wisconsin lab atomic physics group has published transition probabilities in the HPF domain for Ti I (Lawler et al. 2013), and Co I (Lawler et al. 2015). For Fe I a collaboration between investigators at Imperial College London Blackett Laboratory and the Wisconsin group (O'Brian et al. 1991; Ruffoni et al. 2014; Den Hartog et al. 2014; Belmonte et al. 2017) has yielded an extensive set of reliable gf values ranging from the UV to the near-IR. We used only lines from those studies in our Ti, Fe, and Co analyses. This

[4] Available at http://www.as.utexas.edu/∼chris/moog.html

[5] Available at https://github.com/vmplacco/linemake

ensured gf source consistency for these elements in HPF and optical spectra, at the expense of ignoring potentially useful transitions in the HPF region.

Of the remaining 13 species, there are 8 with detected lines in our HPF data that have transition probabilities given in the NIST atomic line database (Kramida et al. 2019)[6]. The NIST atomic line catalog is a critical compilation, and they provide transition probability accuracy assessments. For our lines these quality estimates range from "A+" (uncertainties less than 2%) to "D" (uncertainties less than 50%). We list the NIST line qualities in Table 4. We have included all promising lines without discrimination among NIST quality values, but caution should be observed for those lines with ratings of "C" and lower.

Finally, detected HPF transitions of Ca I, Cr I, Mn I, and Ni I lack recent lab transition work and they do not appear in the NIST database. For these lines we adopted the $gf-$values given in the Kurucz (2011, 2018)[7] semiempirical line compendium. Decades of work by Kurucz have yielded a database of millions of transitions. Pragmatic mixing of results from laboratory and theoretical studies along with fresh computations has produced good matches between stellar observed and predicted spectra, but individual transition probabilities have widely varying accuracies; this should be kept in mind here.

S I deserves a more expanded description. There are several lines in the zyJ spectral domain, and they generally have gf-values available in the NIST database. Table 1 of Spite et al. (2011) lists the most promising transitions in the optical and near-IR regions. In our HPF spectra of RHB stars we have all of these lines except the optical triplet at 6757 Å (see Costa Silva et al. 2020 for a large survey based on those lines). Detections in our spectra include the ground-state [S I] line at 10821.11 Å. Caffau & Ludwig (2007) have explored the use of this transition in solar-type stars. It is an attractive alternative to the high-excitation ($\chi \gtrsim 6.5$ eV) S I lines that are normally studied, because it has little $T_{\rm eff}$ sensitivity and is essentially formed in LTE. However, there are some practical problems with this line for our abundance analyses: (a) the line is very weak; (b) it has an un-identified blend in its red wing (see Figure 1 in Caffau & Ludwig); and (c) it is located only 2 Å from the edge of its HPF spectral order. For the present HPF exploration we drop the 10821 Å line, but it should considered more carefully in future papers.

The S I triplet at 9212.9, 9228.1, and 9237.5 Å is strong and has been used in several S abundance studies (e.g., Spite et al. 2011, Koch & Caffau 2011). In our HPF spectra these lines are useful, but with two cautions. First, they are somewhat saturated in our RHB stars, and the derived S abundances have some dependence on assumed microturbulent velocity V_{mic}. Second, the spectral region surrounding this S I has a large amount of telluric contamination, which is a potential problem with HPF located at McDonald Observatory. The papers cited here were based on data obtained at Chilean observatories, with much less water vapor contaminating the stellar spectra.

The S I triplet near 10457 Å is about half as strong as the 9200 Å one, and for metal-rich giants such as our RHBs these lines are easy to analyze. Finally, Ryde et al. (2019) has identified a line at 10635 Å as a S I transition, particularly for evolved stars with $T_{\rm eff} \gtrsim 5500$ K (see their Figure 1). Preliminary syntheses confirmed its suitability for our study.

In the end, the preliminary synthetic spectrum computations outlined here yielded about 100 atomic lines worthy of further abundance analysis. Most of these were judged relatively uncontaminated by known atomic and molecular blends, and thus could be safely analyzed from their EW measurements. About 20 of the lines were either somewhat blended, or very weak, or have hyperfine structure. For these we performed synthetic spectrum calculations.

3.2. *Equivalent Widths*

For the majority of transitions we derived abundances from EW computations. We measured EWs with the specialized software package *SPECTRE* Fitzpatrick & Sneden (1987)[8]. Interactive fits were made for all lines, with most of them modeled with Gaussian approximations. For the strongest lines, we used empirically-determined Voigt profiles. We also set local continua interactively in this procedure, since the IRAF *continuum* task produce good general fits to each HPF order blaze function but are inadequate for the small spectral intervals surrounding each measured line.

[6] https://physics.nist.gov/PhysRefData/ASD/lines_form.html

[7] http://kurucz.harvard.edu/linelists.html

[8] Available at http://www.as.utexas.edu/~chris/spectre.html

The short wavelength limit for HPF is ∼8080 Å. This overlaps with the long wavelength limit of the optical spectrograph TS23, ∼8900 Å.[9] In the parts of this wavelength domain that are relatively free from telluric absorption (∼8300−8900 Å), we measured *EW*s for RHB stars HIP 33578, HIP 114809, and metal-poor HD 122563 using spectra from both instruments. In Figure 2 we show the *EW* comparisons. The agreement between HPF and TS23 values is at the level of our ability to reliably make *EW* measurements. Decisions on continuum placement and line profile fits cause *EW* measurement scatter at the level indicated by the line-to-line scatter. For the strongest lines, assumptions of appropriate line profile shape (Gaussian or Voigt) also can affect the *EW*s, but the fractional *EW* differences in weak and strong lines are similar. The two spectrographs yield essentially identical spectra of red giant stars.

3.3. *Adopted Model Atmospheres*

The model atmospheric parameters of our science targets have been adopted from our previous efforts (Afşar16, BT16, Afşar18a), in which we describe the derivation of model atmospheres in detail. In summary here, we used a semi-automated version of the MOOG code introduced in §3.1. This driver software begins with information from photometry and spectra line-depth ratios to generate initial model parameter estimates, and then operates iteratively using both neutral and ionized species of Fe and Ti lines to calculate the best model atmospheric parameters. They are listed in Table 3. Typical parameter uncertainties are 150 K for $T_{\rm eff}$, 0.25 for log g and V_{mic}, and 0.1 for [Fe/H]; see Afşar18a §6.3 for a discussion of these values. Optical atomic and molecular line lists that we used to derive atmospheric parameters and individual element abundances were adopted from Böcek Topcu et al. (2015) and BT16.

3.4. *Derived Abundances*

We determined the abundances of most elements by matching their equivalent widths with computed ones, using the stellar atmosphere models (Table 3) and their line parameters (Table 4) described above. Iterations on the output abundances and re-examinations of the spectra resulted in identification and elimination of aberrant lines in individual stars. In Table 5 we give line-by-line abundances in log ϵ units.[10] Program star metallicities [Fe/H] computed from the Fe I and Fe II lines are listed in Table 3. To compute the [Fe/H] values and subsequent abundance ratios [X/Fe] we have assumed the solar abundance set recommended by Asplund et al. (2009).

HPF metallicities of RHB stars are in reasonable accord with those derived from optical data (Afşar18a). In Figure 3 we illustrate the comparisons. The mean difference for Fe I between the two metallicity sets, defined as Δ[Fe I/H] $\equiv \langle$[Fe I/H]$_{\rm HPF}$ − [Fe I/H]$_{\rm opt}\rangle = 0.04$ ($\sigma = 0.06$). Abundances from both spectral regions are based on the same Wisconsin/London group transition probability sources. The comparison for Fe II shows a larger offset, Δ[Fe II/H] = 0.08 ($\sigma = 0.05$). All of the optical and HPF gf-values for Fe II are taken from the NIST database, and nearly all of them originate with a critical compilation by Raassen & Uylings (1998), who considered calculated and experimental transition probabilities in their study. The internal consistency of the Fe II HPF lines is good, since the typical line-to-line abundance scatter in this species is small, $\langle\sigma\rangle \simeq 0.05$ (Table 3). However, the relationship between transition data for these lines and those used in optical analyses should be re-examined if larger surveys are undertaken in the future.

For a few stars in our sample we have optical, HPF zyJ, and IGRINS HK spectroscopic analyses, extending from ∼5000 Å to almost 24,000 Å. In Figure 4 we plot the three abundance sets for HIP 114809. Inspection of this figure reveals agreement among the abundances (Table 3) within the line-to-line scatter. Mean values for Fe I and Fe II range over $\langle$[Fe/H]$_{\rm opt}\rangle = -0.38$ to -0.31, and and $\langle$[Fe I/H]$_{\rm IGRINS}\rangle = -0.32$, $\sigma = 0.04$ (Table 6 in Afşar18b). The mean Fe abundances have similar scatter in other program stars.

The optical and HPF Fe I abundances have been derived with laboratory transition probabilities (O'Brian et al. 1991; Den Hartog et al. 2014; Ruffoni et al. 2014; Belmonte et al. 2017). Unfortunately, there are very few recent laboratory log(gf) values for this species (and for most other species as well) for wavelengths beyond 10,000 Å. Therefore the [Fe/H]$_{\rm IGRINS}$ abundances in Afşar18b were determined with transition probabilities derived from reverse solar analyses. Additionally, the formal σ-values and the appearance of Figure 4 show that the line-to-line scatter is larger in the HPF abundances than in the optical ones. At least two factors may account for this effect. First, on average the near-IR Fe I lines are much weaker than optical and UV ones. They come from relatively weak branches of multiplets, and

[9] The HPF low wavelength limit is defined by the spectrograph setup, whose disperser positions cannot be altered. For TS23 the cross-disperser tilt can be changed to put very long wavelength echelle orders on its CCD detector, but (a) the detector quantum efficiency strongly declines beyond 9000Å; (b) the detector suffers increasing amounts of fringing toward 10000 Å; and (c) telluric H_2O absorption lines are extremely strong in the ∼8850−9850 Å wavelength region.

[10] For elements A and B, [A/B] = log $(N_A/N_B)_\star$ − log $(N_A/N_B)_\odot$ and log ϵ(A) = log (N_A/N_H) + 12.0 . Also, metallicity will be taken to be the [Fe/H] value.

therefore they often have larger transition probability uncertainties than those stronger lines at short wavelengths.[11] Second, all of the HPF Fe II lines occur in the range 8200−9010 Å. In this region the CN contamination can be severe. We have derived Fe II abundances with full synthetic spectra, and discarded lines that appear to be severely blended. Probably future abundance surveys can successfully extract reliable abundances from *EW* analyses of our chosen Fe II lines, but caution is warranted.

3.5. *Abundance Ratios*

Mean abundance ratios [X/Fe] are presented in Table 6, and in Figure 5 we show the trends of [X/Fe] with [Fe/H] metallicity. Carbon abundances are not plotted in this figure; they will be discussed in §3.7. A few general remarks are in order here. First, we re-emphasize that we have enforced single-source transition probability choices for individual species, but there is gf heterogeneity from species to species; see §3.1 for details. Second, we have relied on standard LTE analyses. Our estimates of non-LTE corrections will be presented in §3.6. Third, the total metallicity domain is small, $-0.5 \lesssim$ [Fe/H] $\lesssim 0.0$, including only thin-disk and some thick-disk stars (see Afşar18a for stellar population assessments of RHB stars). Meaningful discussion of Galactic trends awaits analysis of a sample over a much wider metallicity range.

With these cautions in mind, it is clear in Figure 5 that Fe-group elements Ti, Cr, Mn, Co and Ni all have solar abundance ratios, [X/Fe] $\simeq 0$, from HPF spectra as they do in abundance surveys in other spectral regions. Forming averages of these elements for each star, and defining [Fe-group/Fe] $\equiv$ [⟨Ti I,Ti II,Cr I,Mn I,Co I,Ni I/Fe⟩], for the whole Fe group, the mean for the 13 star RHB set is ⟨[Fe-group/Fe]⟩ $= -0.01$ ($\sigma = 0.04$). The Fe-group abundance means for each star are shown in the bottom middle panel of Figure 5, showing no trend with metallicity, as expected from previous Galactic disk abundance surveys (e.g., Reddy et al. 2003, 2006; Bensby et al. 2014, Afşar18a)

The α elements Mg, Si, S, and Ca show a small trend of increasing [X/Fe] values with decreasing [Fe/H]. Defining [α/Fe] $\equiv$ [⟨Mg, Si, S, Ca/Fe⟩], we plot the mean α values for the RHB stars in the bottom right panel of Figure 5. At [Fe/H] $\simeq 0.0$, [α/Fe] $\simeq 0.0$, and for stars with [Fe/H] $\lesssim -0.2$, [α/Fe] $\simeq +0.2$, again in agreement with the trends found in the survey cited above.

3.6. *Non-Local Thermodynamic Equilibrium Computations*

Local thermodynamic equilibrium (LTE) can be an adequate approximation for abundance computations in red giants for ionized majority species, e.g., the lanthanide ions. However, almost all of our HPF transitions arise from neutral species. Most of their parent elements are heavily ionized in line-forming atmospheric levels, and their neutral transitions in the HPF domain arise from high-excitation levels (averaging ∼4.5 eV in our line list), and many of them have deep line cores formed in shallow layers of the atmosphere where photon losses are strong. We expect that some non-LTE corrections are necessary to produce accurate abundances for most of our HPF transitions.

New detailed non-LTE abundance corrections for 13 elements have been published by Amarsi et al. (2020), including Na, Mg, Si, K, and Ca. The abundance corrections discussed in that study were limited to the optical transitions of most interest to the GALAH survey (De Silva et al. 2015). For this paper we have estimated the non-LTE abundance shifts for as many of our HPF transitions as possible using the departure coefficients by Amarsi et al.

The LTE and non-LTE synthetic spectra were computed with *PySME*, the python version of the spectroscopic analysis code *SME* (Piskunov & Valenti 2017). The computations here are initial estimates of the magnitudes of non-LTE effects for each HPF line in a typical RGB star. A more detailed investigation will be carried out in the future.

For now, we feel more confident with the general magnitude of the non-LTE corrections, and so in Table 7 we present mean values, standard deviations, and number of lines involved in the calculations for six neutral species for a typical RHB star and for HD 122563 (to be discussed in §4.4). The entries in this table suggest that for HPF lines in RHB stars the typical non-LTE abundance correction is $\langle\Delta_{corr}\rangle \simeq -0.15$ with a line-to-line scatter $\sigma \simeq 0.10$. In Figure 5 we illustrate the $\langle\Delta_{corr}\rangle$ values with green arrows in the panels for Na, Mg, K, and Ca. It is apparent that in each of these cases the estimated non-LTE shift significantly reduces the apparent LTE-based overabundances.

3.7. *The CNO Group*

[11] This transition probability problem is even more acute in other species, e.g., Fe II, which has a rich spectrum of lines in the *UV* ($\lambda < 3000$ Å), but only relatively weak transitions at longer wavelengths (Den Hartog et al. 2019). Only a few potentially useful (but ultimately discarded) Fe II lines were found in our HPF spectra of RHB stars, and there are none in the IGRINS wavelength region.

Our RHB stars have few CNO strong abundance indicators in the *zyJ* spectral range. There are some easily-identified C I lines, but this species has played only a very minor role in the extensive literature on C abundances in evolved cool stars. Additionally, there are no strong O I or OH lines in this wavelength domain, thwarting any attempt to derive O abundances. Two prominent CN red-system (0−0) bands are seen in the metal-rich stars of Figure 1: the R-branch head at ≃10871 Å and the Q-branch head at ≃10925 Å. But N abundances derived from these bands are dependent on derived or assumed C and O abundances.

Even with these limitations some headway on CNO can be made with HPF spectra. In Table 8 we summarize optical and HPF abundances for the RHB stars and NGC 6940 MMU 105. The data from optical spectra will be reported by Bozkurt et al. (2021, in preparation). That work will give details of the abundance derivations and will include discussion of uncertainties. The final [C_{mean}/Fe] values are based on multiple C indicators: the CH G-band in the 4280−4330 Å range, and C_2 Swan bands with bandheads near 5160 and 5630 Å. Abundances from C I are determined and tabulated by Bozkurt et al. but they do not participate in the C abundance means. The optical N abundances have been determined using C_{mean} abundances derived earlier in concert with the O abundances (from the [O I] line). Carbon isotopic ratios come mostly from the 8004 Å CN feature that is the basis for most $^{12}C/^{13}C$ estimates in red giants.

Abundances from HPF C I transitions in Table 8 are repeated from Table 6. Mean values for the stellar sample have not been computed because star-to-star abundance differences for C, N, and $^{12}C/^{13}C$ are natural in evolved giants. The three sets of C abundances in Table 8 are offset from each other but they do correlate well: $\langle$[$C_{CI,opt}$/Fe]−[$C_{mean,opt}/Fe$]$\rangle$ = +0.10, σ = 0.08; $\langle$[$C_{CI,HPF}$/Fe]−[$C_{CI,opt}/Fe$]$\rangle$ = +0.19, σ = 0.08; and $\langle$[$C_{CI,HPF}$/Fe]−[$C_{mean,opt}/Fe$]$\rangle$ = +0.30, σ = 0.12. The C I HPF lines clearly yield aberrantly high abundances compared to the other values. The uncertainties in the mean differences are consistent with uncertainties in the observations and abundance computations involving C I lines. This issue should be investigated in the future, with attention to accuracy and consistency of transition probability sources, stellar atmosphere parameter dependences, and non-LTE sensitivities of these high-excitation ($\chi \gtrsim 7.5$ eV) transitions.

Abundances of N were determined via synthetic/observed spectrum matches of the CN (0-0) Q-branch wavelength regions, with the redward-degrading bandhead culminating at 10925 Å. The synthetic spectra were generated assuming the optical O and C_{mean} abundances of Table 6. Formally the optical and HPF N abundances agree very well: $\langle$[$N_{CN,HPF}$/Fe]−[$N_{CN,opt}/Fe$]$\rangle$ = +0.01, σ = 0.05. However, the CN transition data used here all come from one recent extensive laboratory study (Brooke et al. 2014), and Sneden et al. (2014) have shown that various CN bands from blue through the near-*IR* yield internally consistent abundance results. The red system (0-0) bands in the HPF region are much stronger than the (2-0) bands near 8000 Å that have dominated CN studies in the optical spectral region. Probably this will enable CN detection in warmer RHB stars than those included in this study.

Finally, we attempted to estimate $^{12}C/^{13}C$ ratios from the ^{13}CN (0-0) Q-branch bandhead that occurs at 10923 Å, almost 3 Å blueward of the ^{12}CN bandhead. However, in our RHB stars the ^{13}CN lines are very weak, and this small spectral region is contaminated by telluric lines that are difficult to remove accurately. Therefore Table 8 lists only nine isotopic ratios, and a couple of these have large estimated uncertainties. For most stars the best conclusion is that the HPF $^{12}C/^{13}C$ values are consistent with, but probably inferior to those derived from the optical (2-0) transitions.

4. STARS OF SPECIAL INTEREST

Afşar18a identified about 150 true field RHB giants out of their original candidate sample of ∼340 stars. Our RHB targets to observe with HPF included two that Afşar18b analyzed with IGRINS H- and K-band spectra, 12 chosen at random from the Afşar18a list, and two that seemed to be worth special attention. Here we discuss these two RHB field stars, the one open cluster giant, and metal-poor HD 122563.

4.1. *HIP 33578: Undiluted Interior CN−Cycle Products on the Surface*

HIP 33578 is an RHB field star that was an unremarkable member of the Afşar18a survey. But that study concentrated on kinematics, Fe metallicities, and limited Fe-group and α element abundance ratios of its RHB sample. Bozkurt et al. (in preparation) will provide much more extensive abundance information on the LiCNO elements that are sensitive to stellar interior fusion cycles and envelope mixing, along with results many other element groups. In this work we have noticed that HIP 33578 is one of the rare metal-rich field giants with a very low carbon isotopic ratio. Fortunately we were also able to obtain an IGRINS H- and K-band spectrum of this star. The optical, IGRINS, and now HPF spectra present a solid observational case for the extreme $^{12}C/^{13}C$ value, as we illustrate in Figure 6. For all

three wavelength regions, the C abundance is the same while the N abundance has been allowed to vary <0.1 dex to best match the observed ^{12}CN and ^{12}CO in each small spectral interval. The best estimate from synthetic/observed spectrum matches from each of these molecular bands is $^{12}C/^{13}C = 3 \pm 1$. This ratio at the surface of HIP 33578 is lower than, but consistent within the observational and theoretical uncertainties, of the interior CN-cycle $^{12}C/^{13}C$ value presented first discussed in detail by Caughlan & Fowler (1962).

Further support comes from the C and N abundances. From Table 8 the mean values for RHB stars excluding HIP 33578 are $\langle$[C/Fe]$\rangle = -0.36$ ($\sigma = 0.14$) and $\langle$[N/Fe]$\rangle = 0.57$ ($\sigma = 0.14$). The optical results for HIP 33578 are [C/Fe] = −0.88 and [N/Fe] = 0.67 (in accord with the HPF N abundance). The 0.5 dex extra depression in C and more modest enhancement of N are consistent with the very low $^{12}C/^{13}C$ of this star.

The LiCNO abundances and carbon isotopic ratio of HIP 33578 are in the domain of the "weak G-Band" (wkG) disk giants (Sneden et al. 1978; Adamczak & Lambert 2013; Palacios et al. 2016). For HIP 33578 Bozkurt et al. (2021, in preparation), supported by our HPF results, have derived log ϵ(Li) < 0.0, [C/Fe] = −0.7, [N/Fe] = 0.7, [O/Fe] = 0.2, and $^{12}C/^{13}C = 3$, while approximate mean values from Adamczak & Lambert (2013) and Palacios et al. (2016) are $\langle \log \epsilon(\mathrm{Li})\rangle$ = 3 to 10, $\langle$[C/Fe]$\rangle \simeq -1.4$, $\langle$[N/Fe]$\rangle \simeq 1.1$, $\langle$[O/Fe]$\rangle = 0.0$, and $\langle ^{12}C/^{13}C\rangle \simeq 3$ to 10. HIP 33578 has evidence of less C→N conversion. This star's Li abundance is very much smaller than the typical wkG giant, but the samples of both Adamczak & Lambert (2013) and Palacios et al. (2016) have stars with no obvious Li enhancement. Our single star cannot provide much new insight into the evolutionary history of this small red giant subclass. However, the RHB status of HIP 33578 is shared by many wkG stars. From its $T_{\rm eff}$ = 5118 K and its photometry and parallax given in Afşar et al. (2018a) we suggest that $\log(L/L_\odot \simeq 2.5$, in the middle of the set of warmer wkG stars shown in the HR diagrams of Palacios et al. (2016) (see their Figures 7 and 8). We tentatively assign HIP 33578 to the wkG subclass.

4.2. *HIP 99789: a rare Red Horizontal Branch Star with Extremely High Lithium*

In contrast to HIP 33578, the RHB star HIP 99789 has ordinary CNO abundances and $^{12}C/^{13}C$ for our RHB sample (Table 8) but an extremely high Li content: log ϵ(Li) $\simeq$ 2.6, close to the interstellar medium value. No other abundance anomaly is evident in this star. However, we have detected an unusually strong He I absorption line at 10830 Å. In Figure 7 we show a montage of our RHB spectra in the wavelength region surrounding the 10830 Å line. This transition arises from a very high-excitation (19.8 eV) metastable level of He I. It has been used extensively in past studies to trace solar/stellar chromospheric activity and wind outflows, and has gained recent attention as a potential indicator of outflows from exoplanet atmospheres (e.g., Ninan et al. 2020). Inspection of Figure 7 suggests that more than half of our RHB sample, 8 out of 13 stars, have extremely little or no detectable He I absorption at 10830 Å. Another three stars, HIP 476, HIP 33578, and HIP113610, have modest He I lines. But HIP 29962 and HIP 99789 have strong 10830 Å absorptions, suggesting substantial chromospheric activity in their atmospheres. We cannot identify any other distinguishing spectroscopic signatures in HIP 99789, but the possible connection between high Li abundance and He I activity is intriguing and should be pursued with a dedicated set of HPF observations of a larger sample of high-Li stars.

Bozkurt et al. (in preparation) will show that HIP 99789 is the most Li-rich member of the Afşar18a sample. However, its appearance among the RHBs may match a recent discovery about evolved stars with high Li. Singh et al. (2019) have determined Li abundances in red giants whose evolutionary status can be assigned to either the first-ascent RG or the red clump on the basis of their asteroseismological properties determined from the Kepler satellite (Mathur et al. 2017). Significant Li abundances can only be found in the He core-burning red clump stars (see their Figure 4). The standard red clump is cooler than the RHB; the highest $T_{\rm eff}$ reported by Mathur et al. for their Li-rich stars is 4999 K, and almost all other stars are cooler than 4900 K. Most of our RHBs have $T_{\rm eff} \gtrsim 5100$ K. But for HD 99789 Afşar18a derived $T_{\rm eff} = 5054$ K and log $g = 2.41$ (Table 3). The temperature is not radically different than those of the Mathur et al. Li-rich sample, and the gravity is in the middle of their log g distribution. HIP 99789 seems to support their assertion that Li enhancement is strongly associated with the He-core burning phase of late stellar evolution.

However, many decades ago Alexander (1967) speculated that red giants could temporarily enhance their Li contents by ingesting companion planets in their bloated envelopes. Some evidence connecting Li-rich giants to planetary systems has accumulated recently, e.g., Adamów et al. (2018) and references therein. HIP 99789 may have one or more stellar or planetary companions, as indicated by its abnormally large apparent spatial acceleration. Close binary companions can influence unresolved spectra by diluting line depths of the primary star, adding in new lines, and producing anomalous RV offsets. None of our targets show signs of being double-line spectroscopic binaries from their

RV cross-correlation functions. But low mass ratio or longer-period companions could still be present in these systems. Recently, Brandt et al. (2019) cross-matched astrometry from *Hipparcos* and *Gaia* DR2 to produce the *Hipparcos-Gaia Catalog of Accelerations* (HGCA), which provides systematics-corrected proper motions spanning a ≈24-year baseline between the two missions. This catalog provides a convenient way to search for tangential accelerations (changes in proper motion) that can be attributed to long-period giant planets, brown dwarfs, low-mass stars, or white dwarfs depending on the amplitude of the acceleration and orbital separation (e.g., Bowler et al. 2020).

Following Brandt et al. (2019), we make use of the *Gaia* and *Hipparcos-Gaia* scaled positional difference proper motions to calculate accelerations in our sample. Among the 17 stars we observed, all except for NGC6940 MMU 105 have *Hipparcos* astrometry and therefore have entries in the HGCA catalog. Four out of these 16 stars have significant astrometric accelerations: HIP 29962 (149 ± 22 m s^{-1} yr^{-1}), HIP 99789 (670 ± 19 m s^{-1} yr^{-1}), HIP 113610 (255 ± 18 m s^{-1} yr^{-1}), and HIP 114809 (76 ± 8 m s^{-1} yr^{-1}). Interestingly, HIP 29962, HIP 99789, and HIP 114809 also have the largest discrepancies (≈4 km s^{-1}) between the RVs measured from the optical Tull data and our HPF spectra, offering further evidence that these stars have companions based on radial accelerations. The limited astrometric and RV sampling makes it challenging to constrain the nature of the companion, but the amplitude of these accelerations suggest that the companions are most likely low-mass stars or perhaps white dwarfs, both of which are not expected to meaningfully impact the spectra and abundances we derive in this study. While no solid connection can be argued between the large Li of HIP 99789 and its abnormally large apparent acceleration, it should be studied in the future.

4.3. *NGC 6940 MMU 105: The First Open Cluster Star With Extremely Broad High Resolution Spectral Coverage*

The cool red giant MMU 105 is a member of the open cluster NGC 6940, and we have previously reported on its chemical composition from optical (BT16) and IGRINS (BT19) spectra. The instrumental setups and observations were like those discussed in §2.2. Model atmosphere parameters, metallicities, and abundance ratios for 12 NGC 6940 giants were determined in similar fashion to that used for the RHB field stars (Afşar18a), with the added advantage of having a reliable color-magnitude diagram (CMD) for the cluster. The optical-region metallicity of MMU 105 ([Fe/H] = −0.15[12] $\sigma = 0.07$) is somewhat smaller than the cluster mean [Fe/H] = −0.02 ($\sigma = 0.06$). Note that MMU 105 is the coolest (4765 K) of the 12 RGs. The IGRINS H- and K-band iron abundance is larger, $\langle$[Fe/H]$\rangle = -0.04$; our new HPF value is more consistent with the optical result. The Fe-group and α elements in this cluster have the abundances of slightly metal-poor disk stars. For elements with $21 \leq Z \leq 30$, $\langle$[Fe-group/Fe]$\rangle = 0.01 \pm 0.14$, and for lighter elements, $\langle[\alpha/\mathrm{Fe}]\rangle = 0.17 \pm 0.07$. The neutron-capture elements ($Z > 30$) appear to be slightly overabundant by an average of about 0.2 dex. From IGRINS data, $\langle$[Fe-group/Fe]$\rangle = 0.15 \pm 0.07$, and $[\alpha/\mathrm{Fe}] = [\langle$Mg, Si, S, Ca/Fe$\rangle] = 0.11 \pm 0.08$. The HPF abundances listed in Table 6 concur with the optical means for these element groups.

The conclusion of BT16 and BT19 from photometric (CMD) and spectroscopic (abundance) evidence is that all 12 RGs including MMU 105 are helium-burning clump stars. The abundance argument begins with carbon isotopic ratios: $^{12}\mathrm{C}/^{13}\mathrm{C}_{optical} = 15^{+3}_{-2}$, $^{12}\mathrm{C}/^{13}\mathrm{C}_{IGRINS} = 23 \pm 3$, and now we can add $^{12}\mathrm{C}/^{13}\mathrm{C}_{HPF} = 15^{+5}_{-2}$. Both optical and IGRINS data reveal underabundances of C and overabundances of N. The HPF N abundances from the (0-0) bandheads agree well with the previous values, and the HPF C I abundances are in accord with the optical and IGRINS abundances after accounting for the systematic C I offset discussed above. The isochrones discussed in BT16 and BT19 suggest that all NGC 6940 RGs are core He-burning red clump stars with mostly undergone canonical first dredge-up. The HPF C, N, and $^{12}\mathrm{C}/^{13}\mathrm{C}$ values should not be the primary data for assessing mixing in NGC 6940 MMU 105, but clearly they are in agreement with our previous optical and IGRINS studies.

4.4. *HD 122563: The Brightest Very Metal−Poor Halo Giant*

The red giant HD 122563 (HIP 068594) is the only very low metallicity member of the Yale Catalog of Bright Stars (Hoffleit & Warren 1995). It was first noted as a high proper motion star (Roman 1955), and was one of the first very metal−poor stars subject to detailed abundance analysis (Wallerstein et al. 1963). Among many noteworthy chemical composition features, HD 122563 has a very large relative oxygen abundance ([O/Fe] ≃ +0.6; Lambert et al. 1974), very low carbon isotopic ratio ($^{12}\mathrm{C}/^{13}\mathrm{C} = 5 \pm 2$; Lambert & Sneden 1977), and weak neutron-capture abundances in an *r*-process pattern (Sneden & Parthasarathy 1983; Honda et al. 2006).

The HD 122563 spectrum portion displayed in Figure 1 has identifications of three Si I lines and one each of H I, Ca I, Sr II. Neglecting the H I Paschen line, these five transitions represent a significant fraction (5/34) of the total

[12] As renormalized to the solar abundances of Asplund et al. (2009); see BT19.

number of lines that we were able to employ in the HD 122563 abundance analysis. This star simply has a metallicity about 500 times lower than the other stars of our study; most absorption lines simply fade into undetectability.

In Table 9 we list the lines employed in our analysis. The same EW and synthetic spectrum analyses described earlier were applied to the HPF spectrum of HD 122563. We imposed the same transition probability restrictions for this star that we used for the other stars of our sample (see §3.1). We adopted the same model atmosphere that was used in the IGRINS spectrum analysis of Afşar et al. (2016). The modest results are presented in Table 10.

The HD 122563 HPF metallicity, [Fe I$_{HPF}$/H] = −2.87 (σ = 0.07), is consistent with optical value: [Fe I$_{opt}$/H] = −2.92 (σ = 0.12), Of the other species entered in Table 10, we draw attention to Si I, S I, and Sr II.

The abundances from Si I lines in all three spectral domains are displayed in Figure 8. The transition probabilities for all the transitions were taken from the NIST database. Si abundances derived from HPF lines perhaps are the most reliable set. Certainly, as discussed in §4.2 of Afşar et al. (2016), the optical abundances may be the least trustworthy: the two strong lines in the blue (3905 Å and 4102 Å) are beset with blending and analytical difficulties, and the yellow/red lines are all very weak ($\log RW \equiv \log(EW/\lambda) \lesssim -5.6$). The zyJ Si I lines in the HPF spectrum yield a mean Si abundance about 0.1 dex higher than do the lines in the IGRINS H- and K-band region. Resolution of this small discrepancy should begin with a comprehensive new transition probability study.

We have detected S I lines in HD 122563, as we illustrate in Figure 9. The triplet of lines near 10457 Å is strong in metal-rich giants such as HIP 114809 (top panel), and the 10455 Å line is blended enough that its abundance must be derived by synthetic spectrum computations. The two strongest lines of the triplet are clearly seen in HD 122563 (bottom panel). We have derived an S abundance from two of these lines and all three of the 9220 Å lines. Our LTE abundance is [S/Fe] = +0.75 (σ = 0.26), and if we apply the non-LTE correction of −0.17 computed by Spite et al. (2011) we get [S/Fe] = +0.58, somewhat larger than their value of +0.42. Further investigation of this abundance with a completely self-consistent models and computational techniques should be pursued in a future investigation.

5. CONCLUSIONS

We have used the Habitable Zone Planet Finder to explore the spectra of red giant stars in the zyJ (8100−12800 Å) wavelength domain. We studied HPF spectra of 13 RHB stars, one open cluster red clump star, and one very metal-poor halo giant. We derived Fe metallicities that are consistent with those determined with optical and H- & K-band high-resolution spectra. Abundance ratios also proved to be generally in agreement with results from other spectral regions, but it is clear that many transitions in the HPF domain need non-LTE computations to yield accurate results.

Our analyses highlighted four special giant stars. HIP 33578 is an RHB with very low C/N and ^{12}C/^{13}C ratios. It is possibly a member of the weak G-band subclass. HIP 99789 is a (perhaps not so) rare Li-rich RHB star. The unique HPF contribution is our discovery that this star has a strong He I 10830 Å absorption feature, perhaps indicative of unusually large atmospheric activity. NGC 6940 MMU 105 is a normal open cluster red clump star; its HPF abundances generally concur with those derived from other spectral regions. Finally, the well-known very metal-poor giant HD 122563 has very few observable features, as expected. Notable among the detections is the 9220 Å S I triplet, yielding an abundance in one of the lowest-metallicity cases.

HPF is dedicated to measuring high-precision radial velocities in M-dwarf stars, but we have shown in this paper that it can be an attractive instrument for investigating the chemical compositions of warmer red giants. Most useful transitions arise from light and Fe-group neutral species. For some elements, e.g., Mg, Si, and S, the abundances from the HPF zyJ spectral region may prove to be superior to those from the optical region.

ACKNOWLEDGMENTS

We thank Noriyuki Matsunaga and George Preston for helpful comments on the manuscript. These results are based on observations obtained with the Habitable-zone Planet Finder Spectrograph on the Hobby-Eberly Telescope. We thank the Resident Astronomers and Telescope Operators at the HET for the skillful execution of our observations of our observations with HPF. The Hobby-Eberly Telescope is a joint project of the University of Texas at Austin, the Pennsylvania State University, Ludwig-Maximilians-Universität München, and Georg-August Universität Gottingen. The HET is named in honor of its principal benefactors, William P. Hobby and Robert E. Eberly. The HET collaboration acknowledges the support and resources from the Texas Advanced Computing Center. We acknowledge support from NSF grants AST-1006676, AST-1126413, AST-1310885, AST-1517592, AST-1310875, AST-1910954, AST-1907622, AST-1909506, and support from the Heising-Simons foundation in our pursuit of precision spectroscopy in the NIR.

This work also used the Immersion Grating Infrared Spectrometer (IGRINS) that was developed under a collaboration between the University of Texas at Austin and the Korea Astronomy and Space Science Institute (KASI) with the financial support of the US National Science Foundation under grants AST-1229522 and AST-1702267, of the McDonald Observatory of the University of Texas at Austin, and of the Korean GMT Project of KASI. Support for this study was also provided by National Science Foundation grant AST-1616040.

Software: linemake (https://github.com/vmplacco/linemake), MOOG (Sneden 1973), IRAF (Tody 1986, Tody 1993), SPECTRE (Fitzpatrick & Sneden 1987), Goldilocks (https://github.com/grzeimann/Goldilocks_Documentation), PySME (Wehrhahn 2019; 10.5281/zenodo.3520617)

REFERENCES

Adamczak, J., & Lambert, D. L. 2013, ApJ, 765, 155

Adamów, M., Niedzielski, A., Kowalik, K., et al. 2018, A&A, 613, A47

Afşar, M., Bozkurt, Z., Böcek Topcu, G., et al. 2018a, AJ, 155, 240

Afşar, M., Sneden, C., Frebel, A., et al. 2016, ApJ, 819, 103

Afşar, M., Sneden, C., Wood, M. P., et al. 2018b, ApJ, 865, 44

Alexander, J. B. 1967, The Observatory, 87, 238

Amarsi, A. M., Lind, K., Osorio, Y., et al. 2020, A&A, 642, A62

Arenou, F., Luri, X., Babusiaux, C., et al. 2018, A&A, 616, A17

Asplund, M., Grevesse, N., Sauval, A. J., & Scott, P. 2009, ARA&A, 47, 481

Belmonte, M. T., Pickering, J. C., Ruffoni, M. P., et al. 2017, ApJ, 848, 125

Bensby, T., Feltzing, S., & Oey, M. S. 2014, A&A, 562, A71

Böcek Topcu, G., Afşar, M., Schaeuble, M., & Sneden, C. 2015, MNRAS, 446, 3562

Böcek Topcu, G., Afşar, M., & Sneden, C. 2016, MNRAS, 463, 580

Böcek Topcu, G., Afşar, M., Sneden, C., et al. 2019, MNRAS, 485, 4625

Bowler, B. P., Cochran, W. D., Endl, M., et al. 2020, arXiv e-prints, arXiv:2012.04847

Brandt, T. D., Dupuy, T. J., & Bowler, B. P. 2019, AJ, 158, 140

Brooke, J. S. A., Ram, R. S., Western, C. M., et al. 2014, ApJS, 210, 23

Caffau, E., & Ludwig, H. G. 2007, A&A, 467, L11

Caughlan, G. R., & Fowler, W. A. 1962, ApJ, 136, 453

Costa Silva, A. R., Delgado Mena, E., & Tsantaki, M. 2020, A&A, 634, A136

De Silva, G. M., Freeman, K. C., Bland-Hawthorn, J., et al. 2015, MNRAS, 449, 2604

Den Hartog, E. A., Lawler, J. E., Sneden, C., Cowan, J. J., & Brukhovesky, A. 2019, ApJS, 243, 33

Den Hartog, E. A., Ruffoni, M. P., Lawler, J. E., et al. 2014, ApJS, 215, 23

Fitzpatrick, M. J. 1993, in Astronomical Society of the Pacific Conference Series, Vol. 52, Astronomical Data Analysis Software and Systems II, ed. R. J. Hanisch, R. J. V. Brissenden, & J. Barnes, 472

Fitzpatrick, M. J., & Sneden, C. 1987, in Bulletin of the American Astronomical Society, Vol. 19, Bulletin of the American Astronomical Society, 1129

Gaia Collaboration, Brown, A. G. A., Vallenari, A., et al. 2018, A&A, 616, A1

Girardi, L. 1999, MNRAS, 308, 818

—. 2016, ARA&A, 54, 95

Girardi, L., Groenewegen, M. A. T., Weiss, A., & Salaris, M. 1998, MNRAS, 301, 149

Halverson, S., Mahadevan, S., Ramsey, L., et al. 2014, in Society of Photo-Optical Instrumentation Engineers (SPIE) Conference Series, Vol. 9147, Ground-based and Airborne Instrumentation for Astronomy V, 91477Z

Hoffleit, D., & Warren, W. H., J. 1995, VizieR Online Data Catalog, V/50

Honda, S., Aoki, W., Ishimaru, Y., Wanajo, S., & Ryan, S. G. 2006, ApJ, 643, 1180

Horne, K. 1986, PASP, 98, 609

Koch, A., & Caffau, E. 2011, A&A, 534, A52

Kramida, A., Yu. Ralchenko, Reader, J., & and NIST ASD Team. 2019, NIST Atomic Spectra Database (version 5.7.1), [Online]. Available: `https://physics.nist.gov/asd` [Aug 11 2020] National Institute of Standards and Technology, Gaithersburg, MD.

Kurucz, R. L. 2011, Canadian Journal of Physics, 89, 417

Kurucz, R. L. 2018, in Astronomical Society of the Pacific Conference Series, Vol. 515, Workshop on Astrophysical Opacities, ed. C. Mendoza, S. Turck-Chiéze, & J. Colgan, 47

Lambert, D. L., & Sneden, C. 1977, ApJ, 215, 597

Lambert, D. L., Sneden, C., & Ries, L. M. 1974, ApJ, 188, 97

Lawler, J. E., Guzman, A., Wood, M. P., Sneden, C., & Cowan, J. J. 2013, ApJS, 205, 11

Lawler, J. E., Sneden, C., & Cowan, J. J. 2015, ApJS, 220, 13

Mahadevan, S., Ramsey, L., Bender, C., et al. 2012, in Society of Photo-Optical Instrumentation Engineers (SPIE) Conference Series, Vol. 8446, Ground-based and Airborne Instrumentation for Astronomy IV, 84461S

Mahadevan, S., Ramsey, L. W., Terrien, R., et al. 2014, in Society of Photo-Optical Instrumentation Engineers (SPIE) Conference Series, Vol. 9147, Ground-based and Airborne Instrumentation for Astronomy V, 91471G

Mathur, S., Huber, D., Batalha, N. M., et al. 2017, ApJS, 229, 30

Metcalf, A. J., Anderson, T., Bender, C. F., et al. 2019, Optica, 6, 233

Ninan, J. P., Bender, C. F., Mahadevan, S., et al. 2018, in Society of Photo-Optical Instrumentation Engineers (SPIE) Conference Series, Vol. 10709, High Energy, Optical, and Infrared Detectors for Astronomy VIII, 107092U

Ninan, J. P., Stefansson, G., Mahadevan, S., et al. 2020, ApJ, 894, 97

O'Brian, T. R., Wickliffe, M. E., Lawler, J. E., Whaling, W., & Brault, J. W. 1991, Journal of the Optical Society of America B Optical Physics, 8, 1185

Palacios, A., Jasniewicz, G., Masseron, T., et al. 2016, A&A, 587, A42

Park, C., Jaffe, D. T., Yuk, I.-S., et al. 2014, in Society of Photo-Optical Instrumentation Engineers (SPIE) Conference Series, Vol. 9147, Society of Photo-Optical Instrumentation Engineers (SPIE) Conference Series, 1

Piskunov, N., & Valenti, J. A. 2017, A&A, 597, A16

Raassen, A. J. J., & Uylings, P. H. M. 1998, Journal of Physics B Atomic Molecular Physics, 31, 3137

Reddy, B. E., Lambert, D. L., & Allende Prieto, C. 2006, MNRAS, 367, 1329

Reddy, B. E., Tomkin, J., Lambert, D. L., & Allende Prieto, C. 2003, MNRAS, 340, 304

Roman, N. G. 1955, ApJS, 2, 195

Roy, A., Halverson, S., Mahadevan, S., & Ramsey, L. W. 2014, in Society of Photo-Optical Instrumentation Engineers (SPIE) Conference Series, Vol. 9147, Ground-based and Airborne Instrumentation for Astronomy V, 91476B

Ruffoni, M. P., Den Hartog, E. A., Lawler, J. E., et al. 2014, MNRAS, 441, 3127

Ruiz-Dern, L., Babusiaux, C., Arenou, F., Turon, C., & Lallement, R. 2018, A&A, 609, A116

Ryde, N., Hartman, H., Oliva, E., et al. 2019, A&A, 631, L3

Shetrone, M., Cornell, M. E., Fowler, J. R., et al. 2007, PASP, 119, 556

Singh, R., Reddy, B. E., Bharat Kumar, Y., & Antia, H. M. 2019, ApJL, 878, L21

Sneden, C. 1973, ApJ, 184, 839

Sneden, C., Lambert, D. L., Tomkin, J., & Peterson, R. C. 1978, ApJ, 222, 585

Sneden, C., Lucatello, S., Ram, R. S., Brooke, J. S. A., & Bernath, P. 2014, ApJS, 214, 26

Sneden, C., & Parthasarathy, M. 1983, ApJ, 267, 757

Spite, M., Caffau, E., Andrievsky, S. M., et al. 2011, A&A, 528, A9

Tull, R. G. 1998, in Proc. SPIE, Vol. 3355, Optical Astronomical Instrumentation, ed. S. D'Odorico, 387–398

Tull, R. G., MacQueen, P. J., Sneden, C., & Lambert, D. L. 1995, PASP, 107, 251

Wallerstein, G., Greenstein, J. L., Parker, R., Helfer, H. L., & Aller, L. H. 1963, ApJ, 137, 280

Yuk, I.-S., Jaffe, D. T., Barnes, S., et al. 2010, in Society of Photo-Optical Instrumentation Engineers (SPIE) Conference Series, Vol. 7735, Society of Photo-Optical Instrumentation Engineers (SPIE) Conference Series, 1

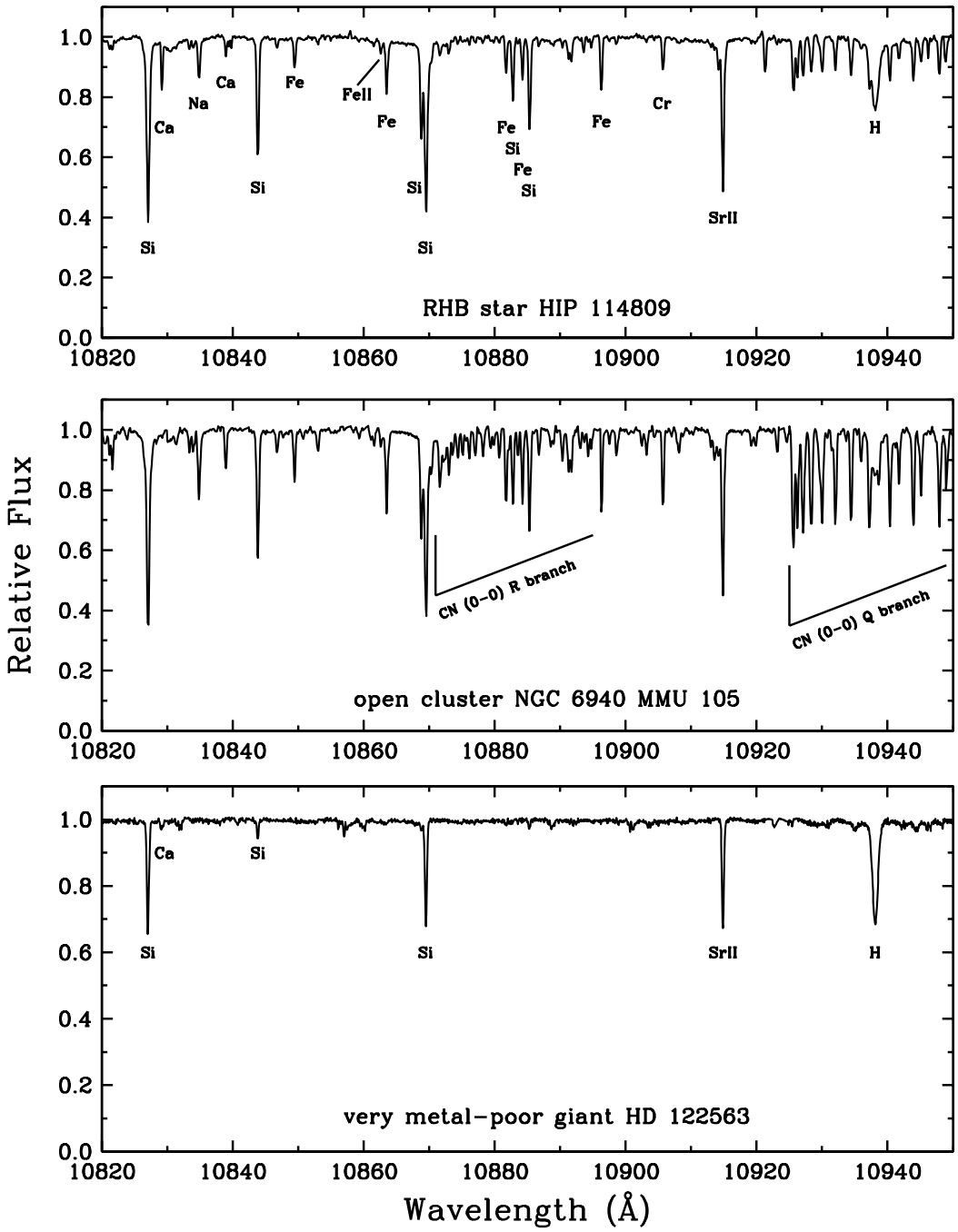

Figure 1. Spectra in an HPF echelle order that has only moderate telluric line contamination (removed in the reduction process described in §2.1). The top panel shows a typical RHB program star, the middle panel has the single cooler−temperature open cluster red clump giant, and the bottom panel has the very metal−poor field giant HD 122563. In the top panel some prominent atomic lines are labeled. All identified lines except Fe II and Sr II are neutral-species transitions. The CN (0−0) R-branch bandhead is also indicated.

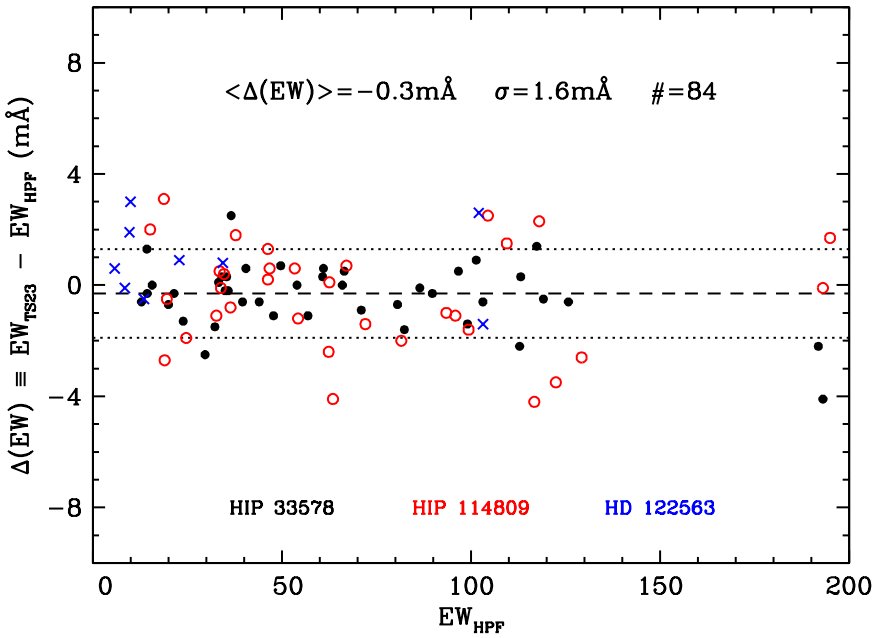

Figure 2. Comparison of equivalent widths measured with the McDonald Observatory TS23 optical echelle spectrograph (Tull et al. 1995) and the HPF. The dashed line represents the mean difference, $\langle\Delta(EW)\rangle = -0.3$ mÅ, and the dotted lines represent the standard deviation of individual measurements $\sigma = 1.6$ mÅ. Three stars, identified in the figure legend, were used for this test. See 3.2 for details.

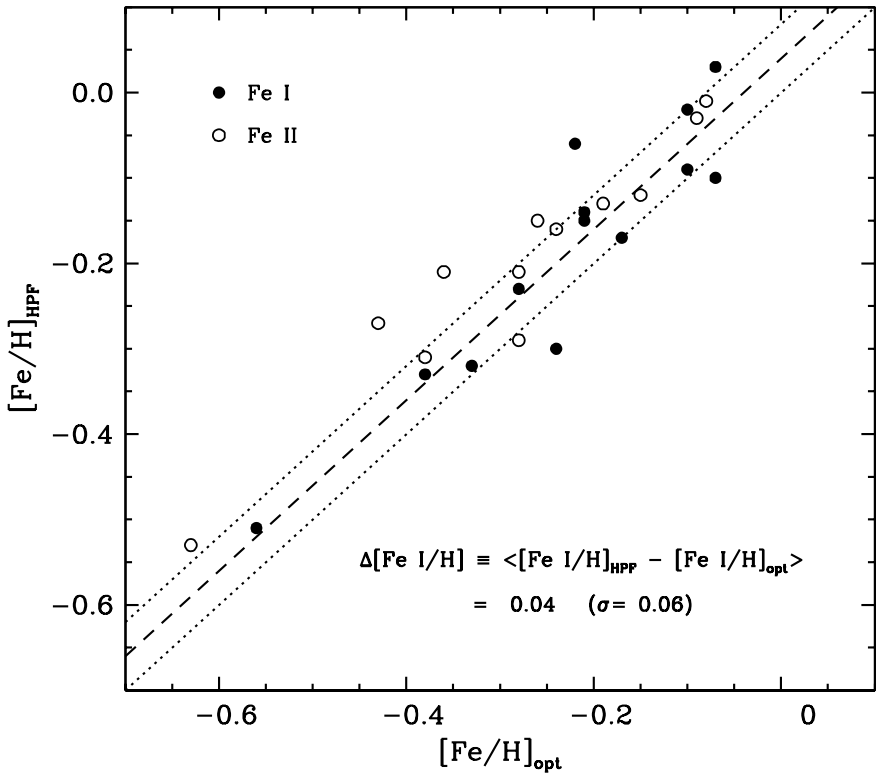

Figure 3. Comparison of Fe I and Fe II metallicities with those from optical spectra Afşar18a after adjustment to the solar abundances of Asplund et al. (2009). The dashed line represents the mean offset between the two Fe I sets, and the dotted lines represent the standard deviation.

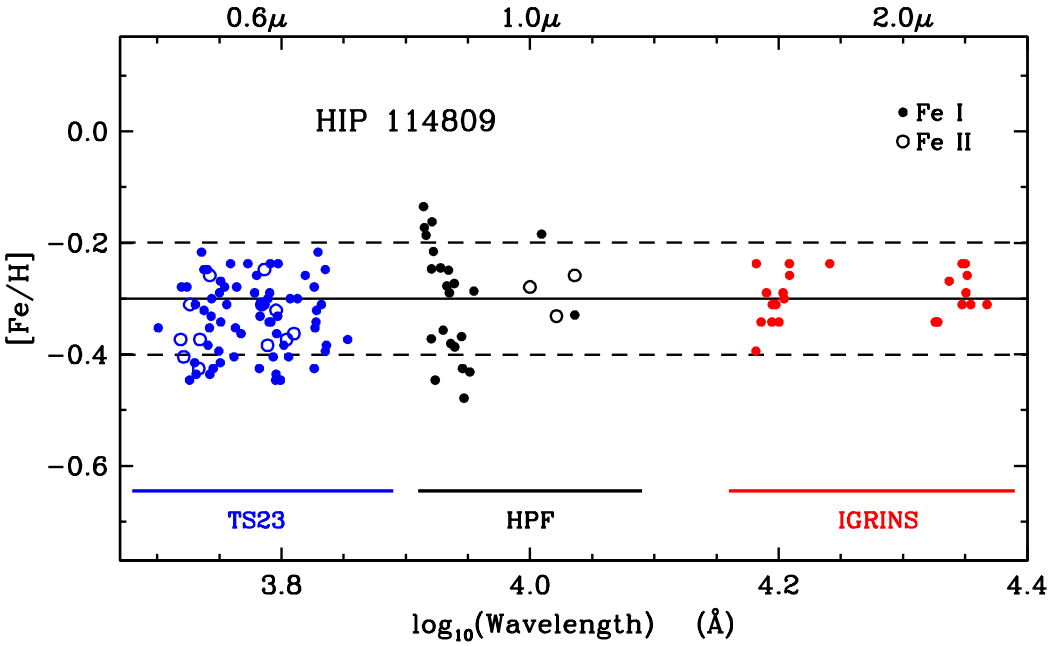

Figure 4. Abundances of Fe lines plotted as a function of wavelength. The wavelength axis is plotted logarithmically due to its large range. Results from optical TS23, HPF, and IGRINS spectra are shown with different colors. The lines denote statistics of the HPF Fe I results; the solid line is for $\langle$[Fe I/H]$\rangle_{\rm HPF}$, and the two dashed lines represent the 1-σ standard deviation for the HPF abundances.

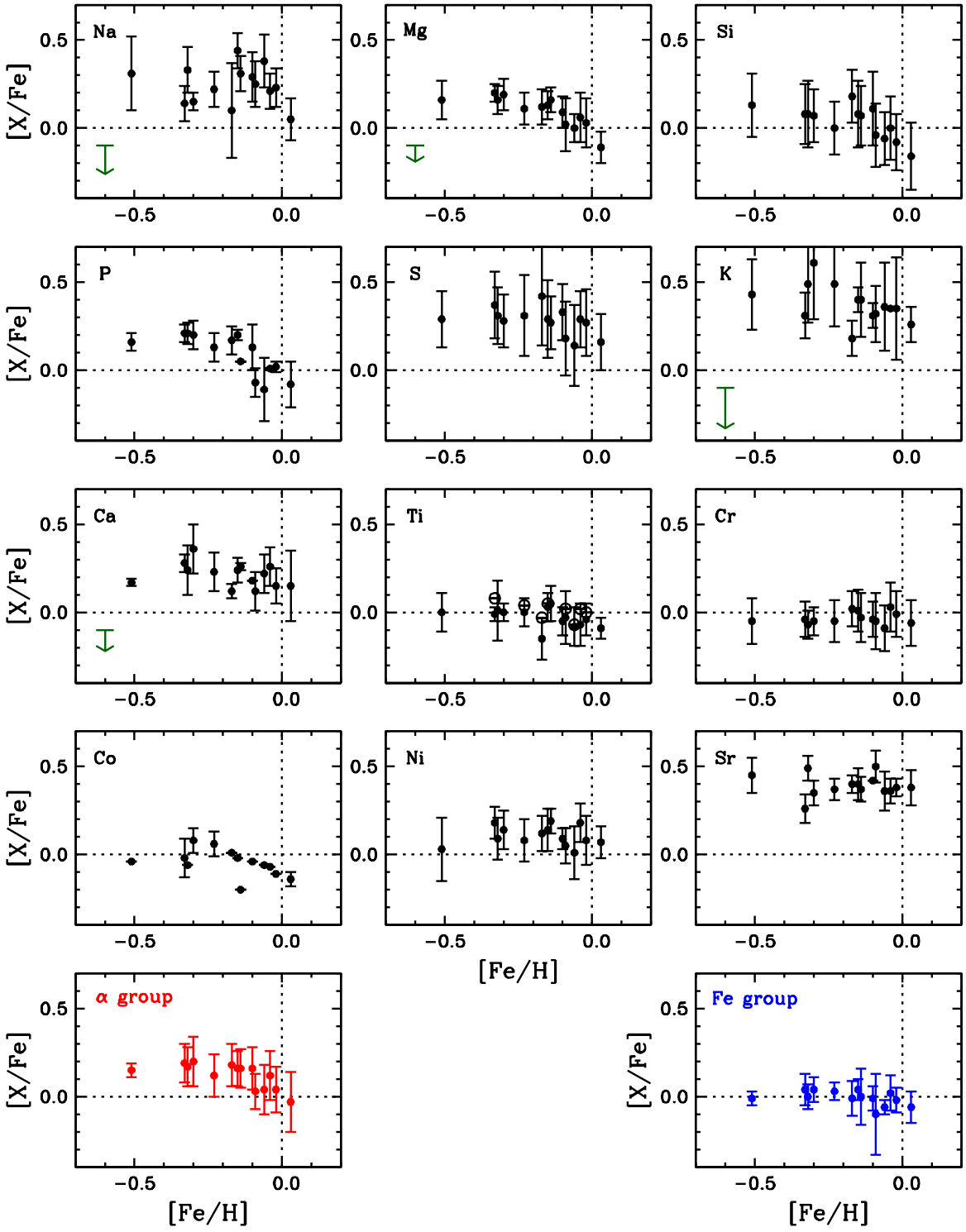

Figure 5. Abundance ratios [X/Fe] plotted as functions of the [Fe/H] metallicity for most elements in this study. The solar values of these quantities, [Fe/H] ≡ 0.0 and [X/Fe] ≡ 0.0, are indicated with dotted lines. In the panel for Ti (middle panel of the figure), the abundances derived from Ti II lines are depicted with open symbols. In the Fe-group (bottom middle) panel, the points are colored blue to emphasize that they are simple means of Ti, Cr, Mn, Co and Ni abundances. In the α-group (bottom right) panel, the points have red colors; they are simple means of Mg, Si, S, and Ca abundances.

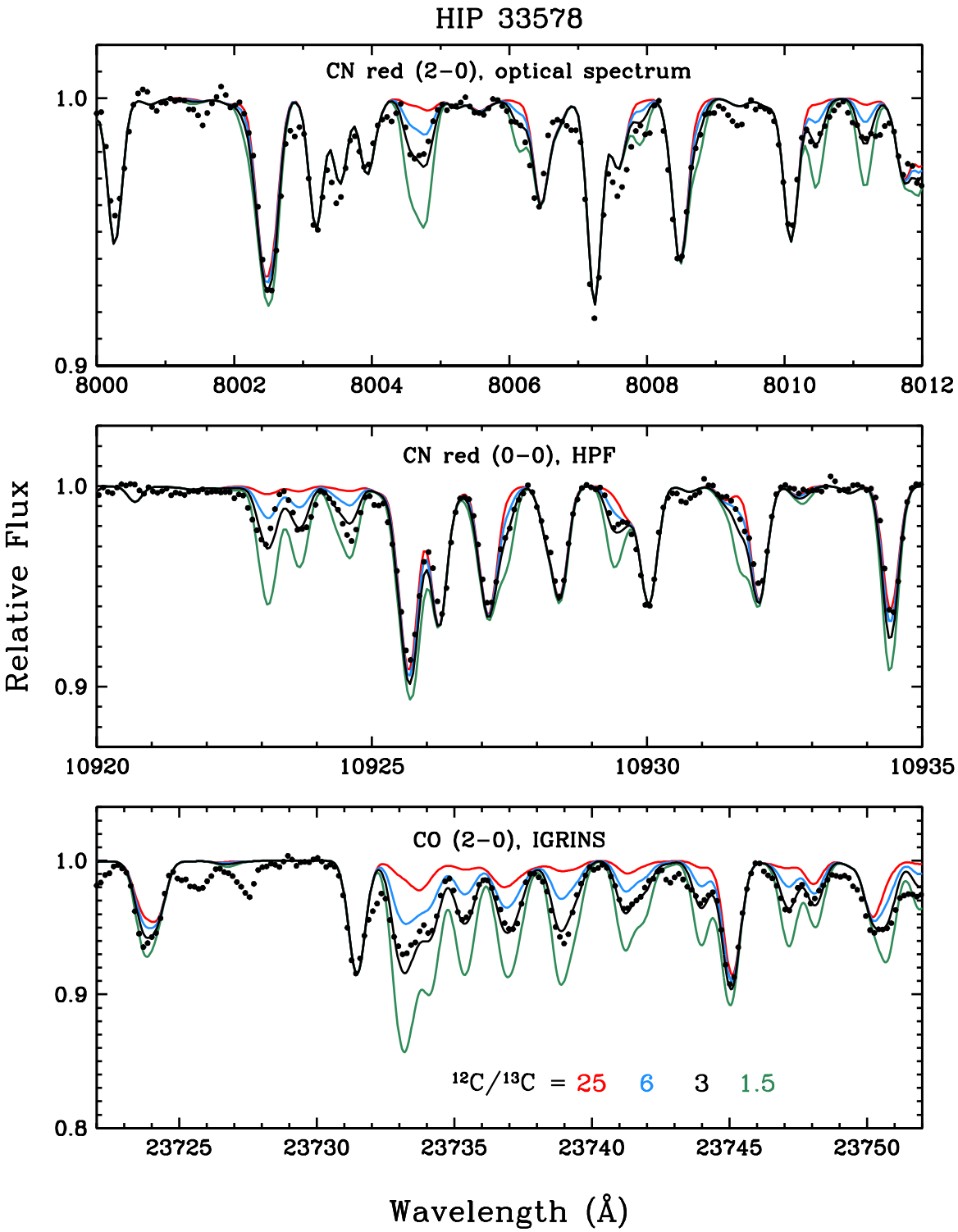

Figure 6. Prominent ^{13}C molecular features in three wavelength domains of HIP 33578. The dots represent the observed spectra, and the lines represent synthetic spectra with $^{12}C/^{13}C$ values defined in the figure legend by the line colors.

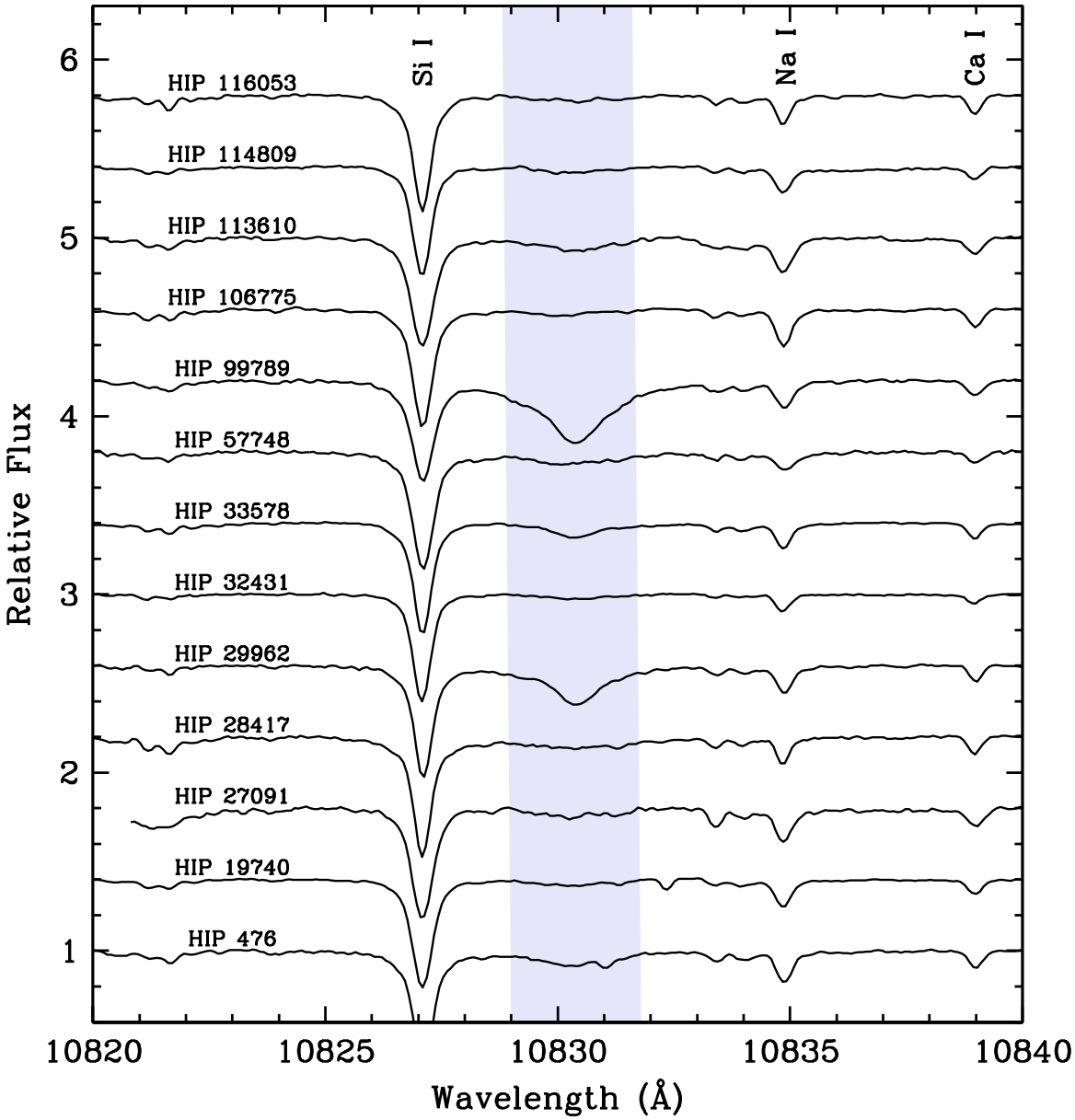

Figure 7. Spectra of the RHB stars surrounding the He I 10830 Å line. The spectra are ordered by star name. The lavender-shaded wavelength area marks the approximate wavelength domain of the broad He I transition. The relative flux scale for HIP 476 is correct, and vertical offsets of 0.4 have been added in succession to the spectra of the other 14 RHBs. Three prominent photospheric absorption lines have been identified, and there are smaller atomic and CN lines that can bee seen in the plot.

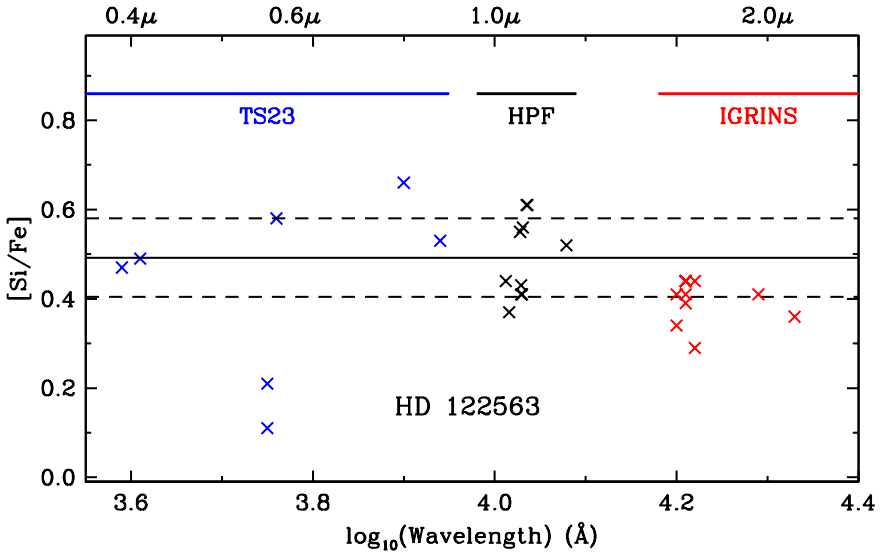

Figure 8. Si abundances from optical (TS23), HPF, and IGRINS data in HD 122563. The solid and dashed horizontal lines show the mean and standard deviation values for the HPF results.

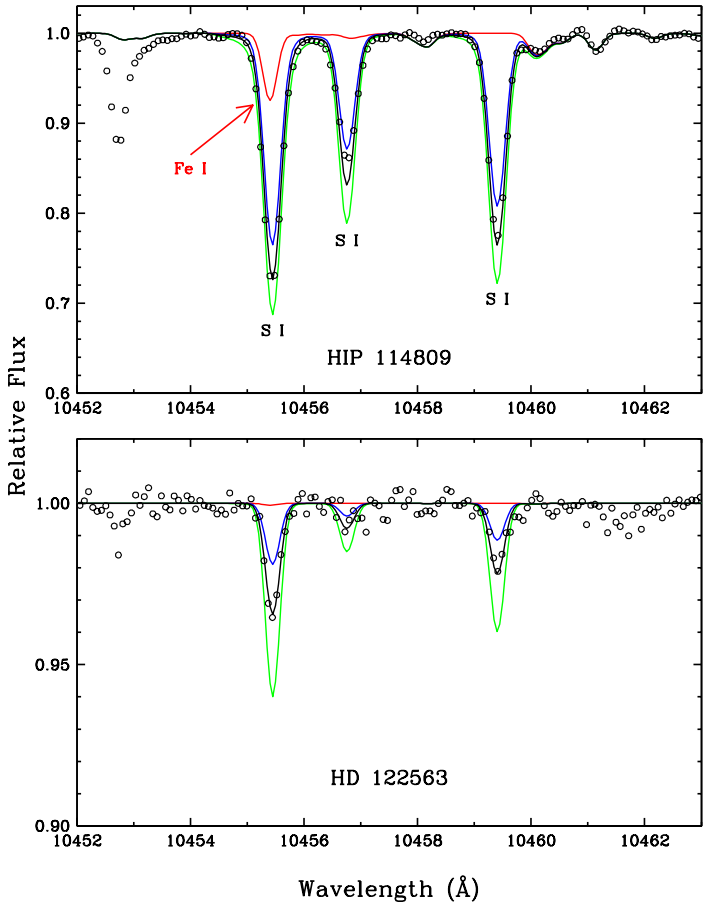

Figure 9. S I in the RHB star HIP 114809 and in the very metal-poor giant HD 122563. In each panel the observed spectra are shown with open circles. The red line represents the synthetic spectrum with no contribution from S I, the black line is for the best overall S abundance, and the blue and green lines are for S abundances that are 0.3 dex smaller and larger than the best abundance.

Table 1. Basic Parameters of Target Stars and Observation Dates

Star Name	RA(2000)[a]	DEC(2000)[a]	B[a]	V[a]	K[a]	d[b]	Date observed
	(h m s)	(° ′ ″)	(mag)	(mag)	(mag)	(pc)	
Observed Targets							
HIP 476	00 05 41.96	+13 23 46.5	6.43	5.55	3.77	122	2018-10-11
HIP 19740	04 13 56.38	+09 15 49.7	5.71	4.89	2.97	128	2018-10-10
HIP 27091	05 44 41.43	+12 24 55.1	7.89	6.94	4.76	291	2018-11-04
HIP 28417	06 00 06.04	+27 16 19.8	7.64	6.62	4.21	145	2018-10-04
HIP 29962	06 18 26.38	+49 11 09.1	8.63	7.74	5.54	199	2018-10-09
HIP 32431	06 46 10.37	+23 22 16.4	7.34	6.49	4.32	221	2018-10-09
HIP 33578	06 58 36.73	−07 11 08.9	7.89	7.13	5.14	145	2018-11-19
HIP 57748	11 50 36.25	+43 39 32.2	8.66	7.90	6.01	210	2019-05-18
HIP 99789	20 14 46.98	+26 47 32.6	9.20	8.33	6.15	470	2018-11-21
HIP 106775	21 37 41.66	+15 12 57.5	8.37	7.44	5.24	358	2018-11-16
HIP 113610	23 00 37.91	+00 11 09.1	7.10	6.23	4.22	183	2018-10-08
HIP 114809	23 15 23.04	+25 40 20.1	7.64	6.81	4.76	209	2018-11-12
HIP 116053	23 30 54.85	+07 59 48.9	9.04	8.10	5.89	243	2018-11-19
NGC6940 MMU 105	20 34 25.46	+28 05 05.6	11.90	10.66	7.82	1021	2019-06-19
HD 122563	14 02 31.84	+09 41 09.9	7.10	6.19	3.73	290	2018-07-17
Telluric Standards							
HR 26	00 10 02.20	+11 08 44.9	5.46	5.53	5.70	93	2018-10-11
HR 1307	04 13 34.56	+10 12 44.9	6.27	6.25	6.03	145	2018-10-10
HR 1808	05 27 10.09	+17 57 43.9	5.30	5.40	5.59	203	2018-11-04
HR 2084	05 57 59.65	+25 57 14.1	4.76	4.82	5.03	476	2018-10-04
HR 2257	06 22 03.55	+59 22 19.5	6.21	6.07	5.51	152	2018-10-09
HR 2529	06 51 33.05	+21 45 40.1	5.26	5.26	5.17	129	2018-10-09
HR 2648	07 02 54.77	−04 14 21.2	4.80	5.00	5.50	373	2018-11-19
HIP 55182	11 17 55.15	+40 50 14.4	8.98	8.93	8.88	345	2019-05-18
HR 7734	20 14 04.88	+36 36 17.5	6.45	6.46	6.36	283	2018-11-21
HR 8258	21 35 27.03	+24 27 07.7	6.35	6.22	5.79	198	2018-11-16
HR 8773	23 03 52.61	+03 49 12.1	4.40	4.52	4.75	125	2018-10-08
HIP 115579	23 24 43.38	+36 21 43.8	6.89	7.02	7.43	413	2018-11-12
HR 8963	23 37 56.80	+18 24 02.4	5.48	5.48	5.42	74	2018-11-19
HR 7958	20 46 38.59	+46 31 54.1	6.36	6.30	6.04	151	2019-06-19
HIP 68209	13 57 52.12	+16 12 07.5	7.65	7.58	7.41	256	2018-07-17

[a] SIMBAD Database

[b] Adopted from Gaia DR2 (Gaia Collaboration et al. 2018)

Table 2. Radial Velocities

Star	RV[a]	σ	RV	σ	RV	σ	δRV	δRV
	HPF	HPF	opt	opt	Gaia	Gaia	opt−HPF	Gaia−HPF
HIP 476	2.06	0.17	2.31	0.12	1.90	0.12	0.25	−0.16
HIP 19740	−7.69	0.23	−7.76	0.18	−7.98	0.14	−0.07	−0.30
HIP 27091	−37.98	0.26	−37.13	0.18	−38.18	0.15	0.85	−0.20
HIP 28417	100.59	0.18	101.21	0.21	100.22	0.18	0.62	−0.36
HIP 29962	11.99	0.14	15.89	0.21	12.13	1.38	3.90	0.14
HIP 32431	41.18	0.15	41.08	0.20	41.15	0.17	−0.10	−0.03
HIP 33578	24.33	0.13	23.04	0.17	24.12	0.20	−1.29	−0.21
HIP 57748	−20.48	0.16	−21.04	0.16	−20.88	0.13	−0.56	−0.40
HIP 99789	−16.90	0.20	−12.90	0.16	−17.96	0.86	4.00	−1.06
HIP 106775	−27.22	0.09	−27.89	0.18	−27.53	0.23	−0.67	−0.30
HIP 113610	−14.48	0.07	−13.75	0.15	−14.53	0.14	0.73	−0.05
HIP 114809	38.13	0.17	41.84	0.19	38.06	0.18	3.71	−0.07
HIP 116053	7.09	0.24	5.05	0.52	7.13	0.18	−2.03	0.04
N6940 MMU 105	9.13	0.20	7.74	0.08	8.38	0.23	−1.39	−0.75
HD 122563	−25.85	0.26	−27.09	0.56	−26.13	0.04	−1.24	−0.28

[a] All velocities are in km s^{-1}

Table 3. Program Star Model Atmospheres

Star Name	$T_{\rm eff}$	log g	V_{mic}	[Fe I]	σ	[Fe II]	σ	[Fe I]	σ	#lines	[Fe II]	σ	#lines
	K		km s^{-1}										
	opt[a]	opt	opt	opt	opt	opt	opt	HPF	HPF	HPF	HPF	HPF	HPF
Field RHB Stars													
HIP 476	5109	2.68	1.36	−0.10	0.07	−0.09	0.04	−0.02	0.14	21	−0.03	0.04	4
HIP 19740	5135	2.51	1.35	−0.10	0.07	−0.15	0.03	−0.09	0.11	22	−0.12	0.03	4
HIP 27091	5001	2.37	1.56	−0.21	0.06	−0.24	0.07	−0.14	0.11	19	−0.16	0.09	4
HIP 28417	4679	2.15	1.42	−0.38	0.06	−0.43	0.05	−0.33	0.12	20	−0.27	0.12	3
HIP 29962	5118	2.92	1.19	−0.28	0.06	−0.36	0.04	−0.23	0.11	20	−0.21	0.08	4
HIP 32431	5125	2.26	1.57	−0.56	0.05	−0.63	0.05	−0.51	0.11	25	−0.53	0.03	4
HIP 33578	5118	2.92	1.19	−0.24	0.06	−0.28	0.05	−0.30	0.15	22	−0.21	0.01	3
HIP 57748	5307	2.34	1.82	−0.17	0.06	−0.19	0.05	−0.17	0.12	22	−0.13	0.05	4
HIP 99789	5054	2.41	1.12	−0.22	0.06	−0.28	0.09	−0.06	0.14	20	−0.29	0.02	4
HIP 106775	5111	2.41	1.61	−0.21	0.05	−0.26	0.06	−0.15	0.14	20	−0.15	0.07	4
HIP 113610	5106	2.39	1.55	−0.07	0.07	−0.04	0.05	−0.10	0.13	19	...	...	...
HIP 114809	5139	2.59	1.31	−0.33	0.06	−0.38	0.05	−0.32	0.10	23	−0.31	0.04	3
HIP 116053	5100	3.09	0.98	−0.07	0.06	−0.08	0.05	0.03	0.13	24	−0.01	0.08	3
Other Stars													
N6940 MMU 105	4765	2.34	1.35	−0.10	0.08	−0.15	0.07	−0.04	0.11	16	0.02	0.03	4
HD122563	4500	0.80	2.20	−2.98	0.07	−2.98	0.07	−2.89	0.03	7	...	...	...

[a] The optical values are taken from high-resolution optical spectroscopy obtained with the McDonald Observatory 2.7m TS23 echelle spectrograph (Afşar16, BT16, Afşar18a).

Table 4. Atomic Lines[a]

λ (Å)	Species	χ (eV)	log(gf)	Source[b]
8335.15	C I	7.679	−0.44	NISTB+
9061.44	C I	7.477	−0.35	NISTB
9094.83	C I	7.482	+0.15	NISTB
9405.73	C I	7.679	+0.29	NISTB+
9658.43	C I	7.482	−0.28	NISTB
10123.87	C I	8.531	−0.03	NISTC+
10683.08	C I	7.477	+0.08	NISTD
10685.34	C I	7.475	−0.27	NISTB
10691.24	C I	7.482	+0.34	NISTB
10707.32	C I	7.477	−0.41	NISTB

[a] The full version of this table in ascii form is available on−line

[b] Sources of the transition probabilities: NIST = the NIST Atomic Spectra Database, https://physics.nist.gov/asd, with notation of their assessment of log(gf) quality; LAWLER13 = Lawler et al. (2013); KURUCZ = the Kurucz (2011, 2018) compendium, http://kurucz.harvard.edu/linelists.html; DENHARTOG14 = Den Hartog et al. (2014); RUFFONI14 = Ruffoni et al. (2014); OBRIAN91 = O'Brian et al. (1991); LAWLER15 = Lawler et al. (2015).

Table 5. Line Abundances[a]

Species	λ (Å)	(1)[b] mÅ	(2) mÅ	(3) mÅ	(4) mÅ	(5) mÅ	(6) mÅ	(7) mÅ	(8) mÅ	(9) mÅ	(10) mÅ	(11) mÅ	(12) mÅ	(13) mÅ	(14) mÅ	(15) mÅ
C I	8335.15	8.18	8.02	8.06	8.21	8.04	7.75	7.67	8.43	7.94	8.13	8.15	8.08	8.17	···	···
C I	9061.44	8.25	7.99	8.30	8.21	8.11	7.96	7.64	8.57	8.18	8.26	8.22	8.19	8.29	···	···
C I	9094.83	8.29	8.09	8.34	8.16	8.16	8.02	7.68	8.64	8.24	8.27	8.30	8.24	8.19	···	···
C I	9405.73	8.17	···	···	8.31	···	7.87	7.69	8.54	···	···	···	8.16	8.12	···	···
C I	9658.43	8.29	8.08	8.25	···	7.99	7.89	7.66	8.65	8.11	8.20	8.22	8.19	8.29	···	···
C I	10123.87	8.26	8.04	8.26	8.30	8.11	7.86	7.55	···	···	8.20	8.15	8.06	8.20	···	···
C I	10683.08	8.21	8.10	8.30	8.11	8.07	7.98	7.67	8.56	8.06	8.21	8.21	8.16	8.13	···	···
C I	10685.34	8.19	8.09	8.27	8.12	8.05	7.89	7.62	8.54	8.04	8.22	8.22	8.13	8.11	···	···
C I	10691.24	8.21	8.10	8.27	8.13	8.02	7.99	7.66	8.56	8.07	8.22	8.24	8.15	8.10	···	···
C I	10707.32	8.18	8.04	8.25	8.16	8.02	7.89	7.62	8.55	8.02	8.19	8.15	8.11	8.16	···	···

[a] The full version of this table in ascii form is available on−line

[b] Star identifications: (1) HIP 476; (2) HIP 19740, (3) HIP 27091; (4) HIP 28417; (5) HIP 29962: (6) HIP 32431; (7) HIP 33578; (8) HIP 57748; (9) HIP 99789; (10) HIP 106775; (11) HIP 113610; (12) HIP 114809; (13) HIP 116043; (14) NGC 6940 MMU 105; (15) HD122563

Table 6. Mean Abundances

Star	C I[a]	Na I	Mg I	Si I	P I	S I	K I	Ca I	Ti I	Ti II	Cr I	Mn I	Co I	Ni I	Sr I
HIP 476[b]	−0.22	0.18	0.03	−0.14	0.02	0.14	0.35	0.15	−0.04	0.00	−0.01	−0.01	−0.11	0.08	0.38
	0.07	0.07	0.14	0.09	0.03	0.04	0.29	0.10	0.09	−1.00	0.13	−1.00	0.00	0.14	0.05
	16	4	11	12	3	4	3	2	6	1	13	1	2	8	3
HIP 19740	−0.30	0.17	0.02	−0.10	−0.07	0.09	0.32	0.12	−0.03	0.02	−0.05	···	−0.51	0.05	0.50
	0.06	0.09	0.15	0.10	0.08	0.08	0.16	0.11	0.15	−1.00	0.16	···	0.07	0.10	0.09
	15	4	10	12	3	4	3	2	6	1	13	0	2	7	3
HIP 27091	−0.09	0.30	0.16	0.01	0.05	0.21	0.40	0.26	0.05	994.19	−0.03	···	−0.20	0.19	0.37
	0.12	0.11	0.07	0.11	0.00	0.12	0.21	0.02	0.10	···	0.14	···	−1.00	0.07	0.07
	15	4	8	11	3	4	2	2	6	0	8	0	1	6	3
HIP 28417	0.09	0.17	0.20	0.03	0.21	0.25	0.31	0.28	−0.01	0.08	−0.04	···	−0.02	0.18	0.26
	0.08	0.08	0.05	0.10	0.05	0.05	0.13	0.05	0.04	−1.00	0.10	···	0.11	0.09	0.08
	15	4	8	12	3	3	3	2	7	1	11	0	2	7	3
HIP 29962	−0.17	0.24	0.11	−0.05	0.13	0.17	0.49	0.23	0.00	0.04	−0.05	···	0.06	0.08	0.37
	0.07	0.10	0.09	0.07	0.08	0.02	0.24	0.11	0.08	−1.00	0.12	···	0.07	0.12	0.06
	15	4	13	13	3	4	3	2	7	1	10	0	2	8	3
HIP 32431	−0.02	0.20	0.16	0.09	0.16	0.16	0.43	0.17	0.00	···	−0.05	···	−0.04	0.03	0.45
	0.07	0.06	0.11	0.13	0.05	0.11	0.20	0.02	0.11	···	0.13	···	0.00	0.18	0.10
	15	4	11	13	3	4	3	2	7	0	8	0	2	6	3
HIP 33578	−0.50	0.23	0.19	0.03	0.20	0.21	0.61	0.36	0.00	···	−0.05	0.03	0.08	0.14	0.35
	0.05	0.05	0.09	0.10	0.08	0.03	0.32	0.14	0.05	···	0.08	−1.00	0.07	0.11	0.07
	16	4	14	14	3	4	3	2	7	0	8	1	2	8	3
HIP 57748	0.25	0.03	0.12	0.13	0.17	0.36	0.18	0.12	−0.15	−0.03	0.02	···	0.01	0.12	0.40
	0.09	0.12	0.10	0.08	0.08	0.15	0.10	0.04	0.12	−1.00	0.10	···	0.00	0.10	0.05
	15	4	12	12	3	4	3	2	2	1	8	0	2	7	2
HIP 99789	−0.30	0.11	0.00	−0.11	−0.11	0.04	0.36	0.22	−0.08	−0.07	−0.09	···	−0.06	0.01	0.36
	0.08	0.09	0.08	0.07	0.18	0.04	0.25	0.11	0.11	−1.00	0.13	···	−1.00	0.15	0.11
	14	4	10	10	3	4	3	2	6	1	10	0	1	7	3
HIP 106775	−0.10	0.44	0.13	0.03	0.20	0.24	0.40	0.24	0.03	0.05	0.01	···	−0.02	0.14	0.40
	0.07	0.12	0.08	0.13	0.03	0.07	0.07	0.07	0.08	−1.00	0.12	···	−1.00	0.12	0.09
	15	4	9	11	3	4	3	2	5	1	11	0	1	9	3
HIP 113610	−0.17	0.41	0.09	0.04	0.13	0.31	0.31	0.18	−0.05	···	−0.04	···	−0.04	0.09	0.42
	0.07	0.12	0.09	0.14	0.13	0.08	0.07	−1.00	0.08	···	0.10	···	0.00	0.06	0.00
	15	4	9	11	3	4	2	1	4	0	7	0	2	5	2
HIP 114809	−0.00	0.29	0.16	0.01	0.21	0.26	0.49	0.24	0.01	···	−0.07	0.05	−0.06	0.09	0.49
	0.07	0.07	0.08	0.11	0.06	0.09	0.22	0.14	0.17	···	0.08	−1.00	0.00	0.12	0.07
	16	4	10	10	3	4	3	2	6	0	11	1	2	8	3
HIP 116053	−0.31	−0.02	−0.11	−0.23	−0.08	0.08	0.26	0.15	−0.09	···	−0.06	···	−0.14	0.07	0.38
	0.07	0.10	0.09	0.10	0.13	0.04	0.10	0.20	0.06	···	0.13	···	0.04	0.09	0.10
	16	4	11	12	3	4	3	2	7	0	12	0	2	8	3
NGC 6940 MMU 105	−0.15	0.27	0.06	−0.06	0.01	0.20	0.35	0.26	−0.07	0.02	0.03	···	−0.07	0.18	0.36
	0.09	0.10	0.14	0.11	0.00	0.05	0.00	0.11	0.12	−1.00	0.14	···	−1.00	0.11	0.07
	12	4	8	12	2	4	2	2	5	1	10	0	1	4	3

[a] The C I mean abundances are tabulated here, but discussion of carbon is referred to 3.7

[b] For each star there are three rows, giving in order the mean abundances, the standard deviations σ, and the number of lines contributing to the means.

Table 7. Mean Non-LTE Abundance Corrections

Species	$\langle\Delta_{corr}\rangle^a$ RHB	σ RHB	#lines RHB	$\langle\Delta_{corr}\rangle^a$ HD122[b]	σ HD122[b]	#lines HD122[b]
C I	−0.15	0.06	16	−0.13	0.00	2
Na I	−0.16	0.19	5	···	···	···
Mg I	−0.09	0.08	11	−0.67	···	1
Si I	−0.19	0.11	14	···	···	···
K I	−0.23	0.15	13	···	···	···
Ca I	−0.12	0.10	2	−0.25	0.07	3

[b] Δ_{corr} is the computed shift for a line need to correct its LTE abundance for non-LTE effects

[b] HD122 = HD 122563

Table 8. LiCNO Abundances

Star	log ϵ(Li)	[C_{CI}/Fe]	[C_{mean}/Fe][a]	[N_{CN}/Fe][b]	[O_{OI}/Fe]	$^{12}C/^{13}C$
			optical spectra			
HIP 476	0.72	−0.35	−0.37	0.62	−0.05	···
HIP 19740	<0	−0.47	−0.54	0.66	−0.11	17
HIP 27091	1.28	−0.25	−0.42	0.73	0.02	20
HIP 28417	<0	−0.02	−0.25	0.33	0.07	12
HIP 29962	<0	−0.23	−0.36	0.61	0.12	20
HIP 32431	<0	−0.12	−0.05	0.58	0.31	20
HIP 33578	<0	−0.72	−0.88	0.67	0.17	3
HIP 57748	<0	−0.04	−0.24	0.40	−0.07	6
HIP 99789	2.61	−0.37	−0.51	0.66	−0.17	13
HIP 106775	<0	−0.22	−0.43	0.76	0.07	13
HIP 113610	<0	−0.46	−0.53	0.53	−0.12	20
HIP 114809	<0	−0.24	−0.35	0.57	0.11	···
HIP 116053	0.42	−0.21	−0.30	0.34	−0.01	17
N6940 MMU 105	<0	−0.27	−0.28	0.41	−0.14	15
			HPF spectra			
HIP 476	···	−0.22±0.07	···	0.54±0.05	···	>20
HIP 19740	···	−0.30±0.06	···	0.70±0.08	···	···
HIP 27091	···	−0.09±0.12	···	0.58±0.08	···	15^{+5}_{-3}
HIP 28417	···	0.09±0.08	···	0.37±0.08	···	10^{+2}_{-2}
HIP 29962	···	−0.17±0.07	···	0.61±0.05	···	···
HIP 32431	···	−0.02±0.07	···	0.58±0.05	···	10^{+5}_{-3}
HIP 33578	···	−0.50±0.05	···	0.68±0.05	···	3^{+2}_{-2}
HIP 57748	···	0.25±0.09	···	0.37±0.05	···	···
HIP 99789	···	−0.30±0.08	···	0.52±0.05	···	···
HIP 106775	···	−0.10±0.07	···	0.70±0.05	···	9^{+4}_{-2}
HIP 113610	···	−0.17±0.07	···	0.61±0.10	···	···
HIP 114809	···	0.00±0.07	···	0.56±0.05	···	10^{+10}_{-3}
HIP 116053	···	−0.31±0.07	···	0.24±0.08	···	25^{+10}_{-5}
N6940 MMU 105	···	−0.15±0.09	···	0.39±0.05	···	15^{+5}_{-2}

[a] The optical mean C abundances are based on CH and C_2 features.

[b] Both optical and HPF N abundances assume the C and O abundances determined from optical [O I] transitions.

Table 9. HD 122563 Line Abundances[a]

Wavelength Å	Species	χ eV	$\log(gf)$	$\log \epsilon$	Source[b]
10683.08	C I	7.477	0.08	5.38	NIST D
10691.24	C I	7.482	0.35	5.53	NIST B
8806.76	Mg I	4.343	−0.14	5.29	NIST A
10288.94	Si I	4.916	−1.48	4.96	NIST C+
10371.26	Si I	4.926	−0.71	4.94	NIST C+
10660.91	Si I	4.916	−0.32	5.22	NIST C+
10689.72	Si I	5.949	0.09	5.35	NIST C+
10694.25	Si I	5.959	0.26	5.37	NIST C+
10727.41	Si I	5.979	0.42	5.41	NIST B
10749.38	Si I	4.926	−0.27	5.23	NIST C+

[a] The full version of this table in ascii form is available on−line

[b] As defined in Table 5

Table 10. HD 122563 Mean Abundances

Species	$\langle$[X/Fe]$\rangle$	σ	#lines
C I	−0.11	0.11	2
Mg I	0.56	···	1
Si I	0.49	0.09	10
S I	0.75	0.26	5
Ca I	0.40	···	1
Ca II	0.54	0.02	2
Ti I	0.23	0.12	3
Fe I	−2.87[a]	0.07	10
Sr II	0.45	0.14	3

[a] For Fe I we quote the metallicity [Fe/H].